energies

MDPI

Article

Comprehensive Dynamic Modelling and Control Strategy Development for Operational Flexibility of a Solid Oxide Electrolyser System

Michele Bolognese [1,*], Luca Pratticò [1], Matteo Testi [1], Emanuele Martinelli [1], Luigi Crema [1] and Nirmala Nirmala [2]

[1] HyRES Unit, Fondazione Bruno Kessler, Via Sommarive 18, , 38123 Trento, Italy; prattico@fbk.eu (L.P.); testi@fbk.eu (M.T.); emmartinelli@fbk.eu (E.M.); crema@fbk.eu (L.C.)

[2] Modelon AB, Ideon Science Park, Scheelevägen 17, 223 70 Lund, Sweden; nirmala.nirmala@modelon.com

* Correspondence: mbolognese@fbk.eu

Abstract

A solid oxide electrolyser coupled to photovoltaic (PV) power operates through production, hot standby and night states. A Modelica model of the balance of plant of the 25 kW PROMETEO pilot is presented, with ten control loops and a hysteresis-based state machine dispatched by the PV power of a grid-connected plant. The stack model, validated on 5 kW data from the FBK laboratories, is scaled up to 25 kW. The constant-voltage, temperature-tracking strategy is simulated over clear-sky, intermittent-cloud and satellite-derived PV days. At 1.32 V/cell, the stack heat-balance point, the sweep air rests at its minimum and the current is tracked through the inlet temperatures alone, giving 14.1 kg of hydrogen over two days at 44 kWh/kg, 65% covered by the PV. The feasible voltage window is narrow: below 1.30 V/cell the stack exceeds 780 °C and above 1.34 V/cell the current becomes steam-limited, requiring a current or steam protection. The strategy is robust to the stack thermal capacity, the PV field size and a ±20% change in the area-specific resistance, which shifts the operating temperature by about 20 K. The sweep-air loop must be disabled outside production; otherwise, blower and heaters saturate and the stack cools.

Keywords: solid oxide electrolysis; balance of plant; dynamic modelling; Modelica; control strategy; photovoltaic-dispatched hydrogen production

1. Introduction

Intermittent renewable energy sources (RESs) require complementary storage to keep the grid stable [1–4]. Hydrogen is an attractive carrier because it is carbon-free [5] and efficiently converted in electrochemical devices [6,7]; it stores renewable electricity in chemical form [8] and supports the decarbonisation of transport, microgrids and industry [9–12]. Water electrolysis is the dominant route to high-purity hydrogen [13], with a share projected to rise from 4% [5] to 51% of hydrogen production by 2050 [14]. Among the technologies, solid oxide electrolysis cells (SOEC) benefit from a high operating temperature (680–1000 °C), which improves kinetics, and from waste-heat integration, which can reduce the electricity consumption per kilogram of hydrogen by up to 30% [15]; in SOEC balance-of-plant (BoP) configurations the sweep-air flow governs both the stack temperature and the pressure losses of the heat-exchanger network [16].

Because of the fluctuating RES input, the plant undergoes frequent transients be-

Academic Editors: Song Li and Ivan Tolj

Received: 14 September 2026
Revised: 12 October 2026
Accepted: 19 October 2026
Published: 22 October 2026

Copyright: © 2026 by the authors. Licensee MDPI, Basel, Switzerland. This article is an open access article distributed under the terms and conditions of the Creative Commons Attribution (CC BY) license.

tween full and partial load and between production and standby, so dynamic models of heat transfer, fluid flow and electrochemistry are needed to design the control strategy. Yin et al. [17] analysed the response of an SOEC system to inlet temperature and flow variations; Saeedmanesh et al. [18] coupled an SOEC with PV input under feedback control; Botta et al. [19] developed PI control for a reversible system; Zhang et al. [20] reduced consumption through thermal control. These works treat the production state and do not address standby and idle states or the supervisory logic that sequences them. A complementary steady-state and annual analysis of the PROMETEO concept, scaled to 100 kW, has been reported by Barreto et al. [21], treating each mode in the steady state; the control options for the pilot were defined by Crespi et al. [22] from a 5 kW test campaign.

This work presents a dynamic model of the complete 25 kW PROMETEO system, stack and BoP, developed in the Modelica language [23] with Modelon Impact 2.1.25 (Modelon AB, Lund, Sweden) and the Modelon, Fuel Cell and Thermal Power libraries [24], chosen for the equation-based, acausal handling of the bidirectional couplings between stack and BoP. The second control option of [22], constant voltage with steam fixed per state and load tracked through the stack temperature, is implemented and verified over a clear-sky day and a synthetic intermittent-cloud day. The contribution is threefold: the dynamics of the complete BoP are resolved across production, hot standby and night mode under a PV-dispatched supervisory logic with hysteresis; the feasible window of the constant-voltage strategy is identified through sensitivity analyses on the stack voltage and on the stack thermal capacity; and a control-structure requirement invisible to steady-state or production-only analyses is exposed, namely that the sweep-air loop must be disabled outside production and coordinated with the temperature references. The aim is to identify inconsistencies in process and control design ahead of commissioning.

2. Methodology

2.1. The PROMETEO System and Its Operating States

The PROMETEO project targeted a 25 kW pilot plant at an existing PV facility in Cuenca, Spain, integrating an SOEC BoP with PV electricity and solar thermal heat, so that hydrogen production is decoupled from heat availability. The BoP comprises four functional zones: steam generation from the solar heat-transfer-fluid (HTF) loop, mixing and preheating of fuel and air by waste-heat recovery, hydrogen production in the stack, and hydrogen post-treatment, recirculation and storage. Three supervisory states are defined (Table 1). In production operating mode, the stack is connected at constant voltage and the load follows the PV power continuously between 150 and 256 A; the steam flow is set at one of two levels according to the current target, 1.50 g/s below 185 A and 2.56 g/s above, sized for a steam utilisation of 75% at 150 and 256 A (54–92% in between). In hot standby (HSB) the stack is disconnected while steam flow, hydrogen fraction and stack temperature are maintained; in night mode (NM) steam is stopped and a forming-gas mixture (N_2/H_2 80/20 vol.) is recirculated to protect the electrodes.

Table 1. Operating states, cathode feed and electrical condition (volume fractions of the cathode feed; steam utilisation from Equation (7)).

State	Cathode Feed (kg/s)	$H_2/H_2O/N_2$ (vol. %)	Electrical Condition	Current (A)	Steam Utilisation (%)
Production, full-load	steam 2.56 × 10^{-3} + H_2	10/90/0	105.6 V (1.32 V/cell)	185–256	54–75

State	Cathode Feed (kg/s)	$H_2/H_2O/N_2$ (vol. %)	Electrical Condition	Current (A)	Steam Utilisation (%)
steam level (target > 185 A)	make-up				
Production, partial-load steam level	steam 1.50×10^{-3} + H_2 make-up	10/90/0	105.6 V	150–185	75–92
Hot Standby	steam 1.50×10^{-3} + H_2 make-up	10/90/0	disconnected	0	n/a
Night Mode	forming gas 0.7×10^{-4} + recirculation 6.3×10^{-4}	20/0/80	disconnected	0	n/a

2.2. Balance-of-Plant Model

Fluid properties are handled through Modelon media models and NASA Glenn coefficients [25]: Water IF97 [26], Therminol 66 [27], the seven-species ideal-gas mixture NasaReformateLong, its condensing extension and NasaMoistAir [20], with medium converters at the zone boundaries [28]. Figure 1 shows the process flow diagram. Steam is raised in the generator (E102) from the solar HTF, with demineralized water at 3 bar preheated in the economizer (E101); the steam flow is modulated by a lamination valve and the drum pressure by the HTF flow. Steam superheating and air preheating take place in the plate heat exchangers (HEX) (E103 and E104) by recovery from the stack off-gases. Downstream of E103 the steam is mixed with a hydrogen-rich stream recirculated from the cold BoP, where it has been cooled, dewatered in the water knock-out (WKO) and recompressed, to give 10% hydrogen in the cathode feed. Dry air is the anode sweep gas, and electric heaters upstream of both inlets bring the streams to the stack inlet temperature.

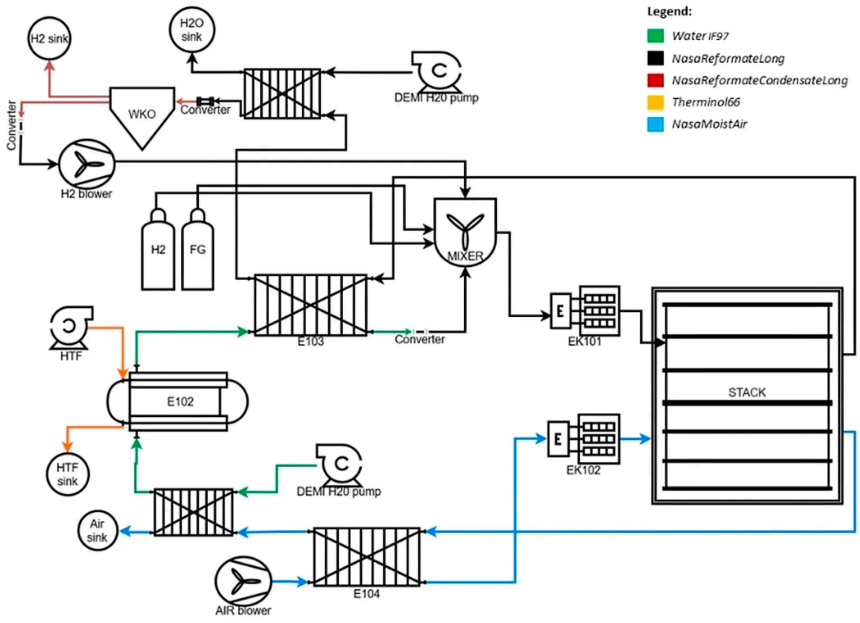


Figure 1. Process flow diagram of the BoP of the hydrogen production plant.

The stack and the heat exchangers are one-dimensional models discretized along the flow ($n = 5$ for the stack, $n = 3$ for the gas/gas HEX); the steam drum, the condensing separator and the cold-side gas volumes are lumped dynamic volumes; valves, blowers and sources are algebraic. All components except the stack are adiabatic; the stack exchanges heat with the 25 °C environment through a multilayer insulation model. The component list, modelling approach and parametrization are given in Appendix A (Table A1) and Appendix F (Table A5); the layout in Modelon Impact is shown in Figure 2 . The stack voltage is imposed by an ideal source. The solar HTF loop is a constant-temperature source at 200 °C, consistent with the molten-salt thermal store interposed between the solar field and E102; with steam raised at 3 bar (133.5 °C) and an HTF flow of 0.10 kg/s at full load, one fifth of the pump range, a 30 K drop of the HTF temperature would be absorbed by a 60% increase in the flow. The stack disconnection is an instantaneous Boolean event. The sweep-air blower is an ideal mass-flow source bounded at 0.002–0.040 kg/s, with its consumption estimated from the network pressure drop with blower and motor efficiencies of 0.55 and 0.90 (Equation (15)). The stack has a lumped thermal capacity of 25 kJ/K, i.e., 50 kg of cell and interconnect material at 500 J/(kg K), distributed over the five segments, while the HEX walls are massless, so that the stack is the only thermal inertia of the hot zone; a direct electric heater on the stack body, as installed on the pilot, is included with its own loop (Section 2.5).

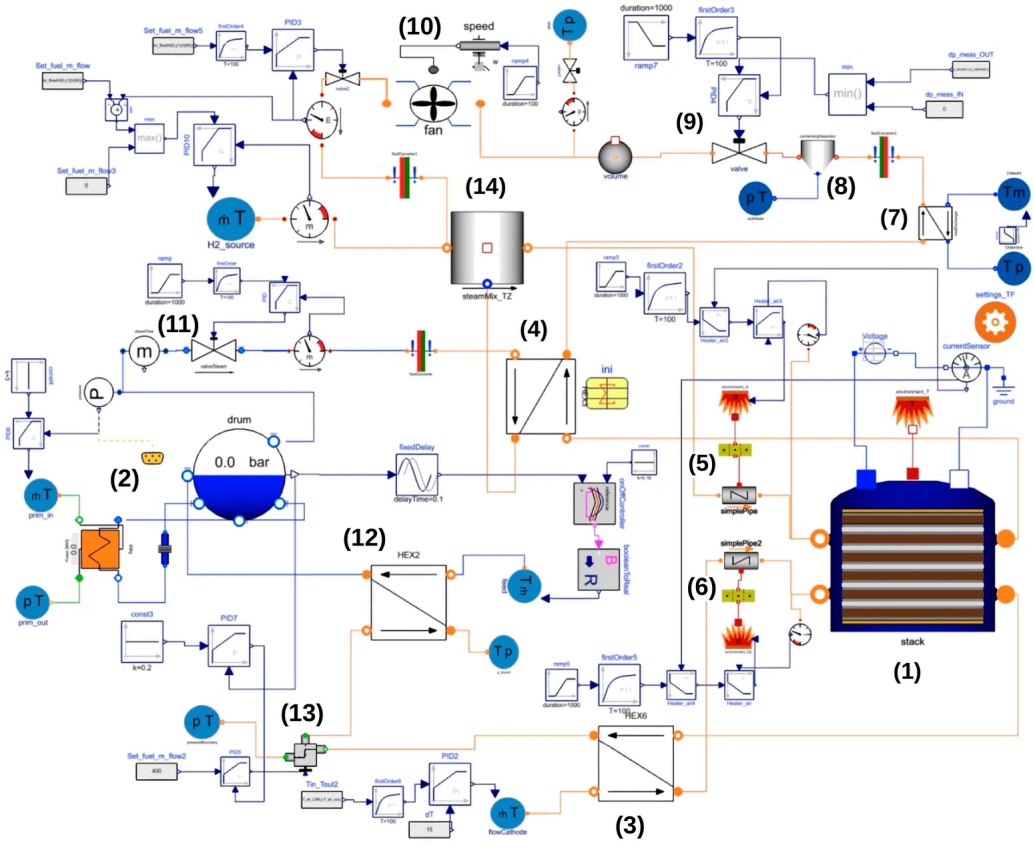


Figure 2. Layout of the complete model in Modelon Impact.

2.3. Stack Model

The elementary cell model of the Fuel Cell Library (Figure 3) lumps the n_cell = 80 series-connected cells and is discretized in N = 5 segments along the flow. Electrically, each segment is a branch with a voltage source and an internal resistance; the N branches are in parallel between the stack terminals, so that all segments share the termi-

nal voltage while the current divides according to local temperature and composition. The open-circuit voltage of a segment is the Nernst voltage of the water-splitting reaction [19]:

$$H_2O \rightarrow H_2 + \frac{1}{2}O_2 \tag{1}$$

$$E_0 = \frac{\Delta G_r\left(T_{cell}\right)}{2F} + \frac{R\ T_{cell}}{2F}\ ln\left(\frac{p_{H_2}\ p_{O_2}^{0.5}}{p_{H_2O}\ \left(p^0\right)^{0.5}}\right) \tag{2}$$

where F is the Faraday constant, p^0 = 1 atm and ΔG_r(T_cell) is the Gibbs free energy of the reaction expressed int he Equation(1), evaluated from the formation properties of the species [25] (about 188 kJ/mol at 800 °C, i.e., 0.98 V); the partial pressures are those of the segment (Appendix E). Under load the overvoltage of a single cell is

$$V_{ohm} = ASR\ j \tag{3}$$

where j is the local current density and ASR the total area-specific resistance, which lumps the ohmic, activation and concentration contributions as in [21,29]: the cell is the simplified electrochemical model of the Fuel Cell Library [30], in which the activation and concentration loss sub-models are set to zero and all internal losses are lumped in the Arrhenius ASR of the ohmic sub-model, so that the segment voltage is given by Equations (2) and (3) alone. The terminal voltage and the stack current follow from the series connection of the cells within a segment and the parallel connection of the branches:

$$V_{stack} = n_{cell}\ (E_0 + V_{ohm}) \tag{4}$$

$$j = \frac{N\ I_j}{A_{cell}}, \qquad I = \sum_j I_j, \qquad R_{int} = \frac{n_{cell}\ N\ ASR}{A_{cell}} \tag{5}$$

with I_j the current of segment j and A_cell/N its area; Equation (5) defines the internal resistance R_int = n_cell N ASR/A_cell identified from the polarisation curves (Section 2.4). The ASR follows an Arrhenius law with respect to T_0 = 1073 K [17]:

$$ASR\ = ASR_0\ exp\left[\frac{E_a}{R}\left(\frac{1}{T_{cell}} - \frac{1}{T_0}\right)\right] \tag{6}$$

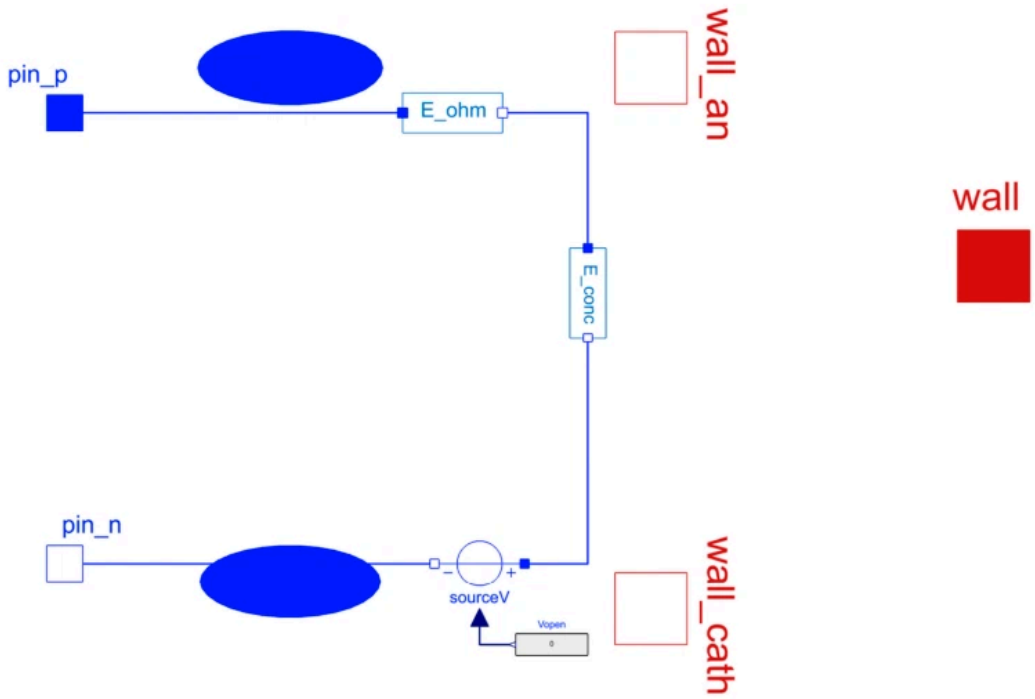


Figure 3. Elementary cell model.

The steam utilisation is the ratio between the water consumed, from Faraday's law for the n_cell cells, and the steam fed to the stack,

$$U_{steam} = \frac{n_{cell}\, I\, MM_{H_2O}}{2F\, \dot{m}_{steam}} \times 100 \tag{7}$$

where MM_H_2O is the molar mass of water and $\dot{m}$_steam the inlet steam flow; the same expression per segment gives the local utilisation. The species exchanged with the channels follow from Faraday's law in each segment,

$$\dot{n}_{k,j} = \nu_k\, n_{cell}\, \frac{A_{cell}}{N}\, \frac{j}{2F} = \nu_k\, n_{cell}\, \frac{I_j}{2F} \tag{8}$$

with $\nu = -1$ for H_2O and +1 for H_2 at the cathode and $\nu = 1/2$ for O_2 at the anode. The library uses the fuel-cell sign convention, so that the stack current I_SOE is negative in electrolysis and its absolute value is used in the balances, and the hydrogen production is

$$I = |I_{SOE}| = -I_{SOE} \tag{9}$$

$$\dot{n}_{H_2} = n_{cell}\, \frac{I}{2F} \tag{10}$$

The electrical power of a segment is P_j = V_stack I_j; the cell energy balance and the enthalpy flows exchanged with the channels are given in Appendix E.

2.4. Stack Calibration, Validation and Scale-Up

The stack parameters ASR_0 and E_a were calibrated on the experimental data of Figure 4 and the calibrated model was validated on the polarisation curves of Figure 5. Figure 4 shows the voltage versus steam utilisation measured on the 5 kW test bench of the FBK laboratories reported by Crespi et al. [22]. The tests were carried out on a G8-80 stack (SolydEra S.p.A., Mezzolombardo, Italy) of 70 cells with an active area of 80 cm^2 each, operated at ambient pressure and at temperatures between 680 and 780 °C. The steam flow was varied stepwise from 360 to 1900 g/h, with inlet temperatures from 670 to 760 °C and 10% hydrogen in the feed, while the voltage was held close to the thermoneutral value and the current was recorded as the measured output

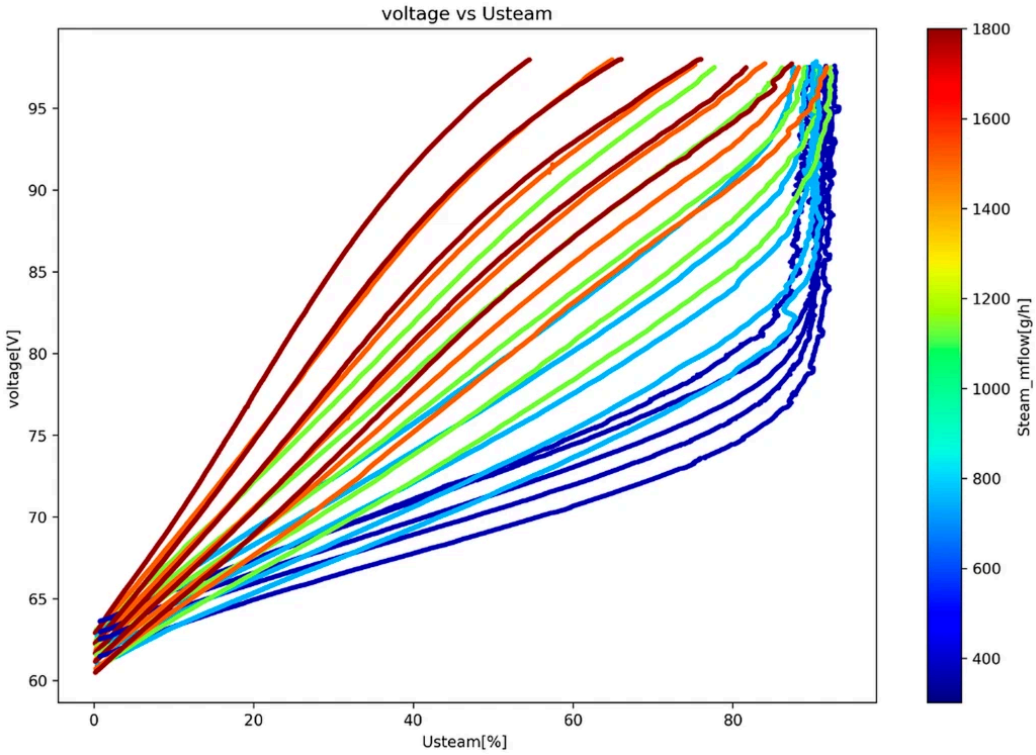
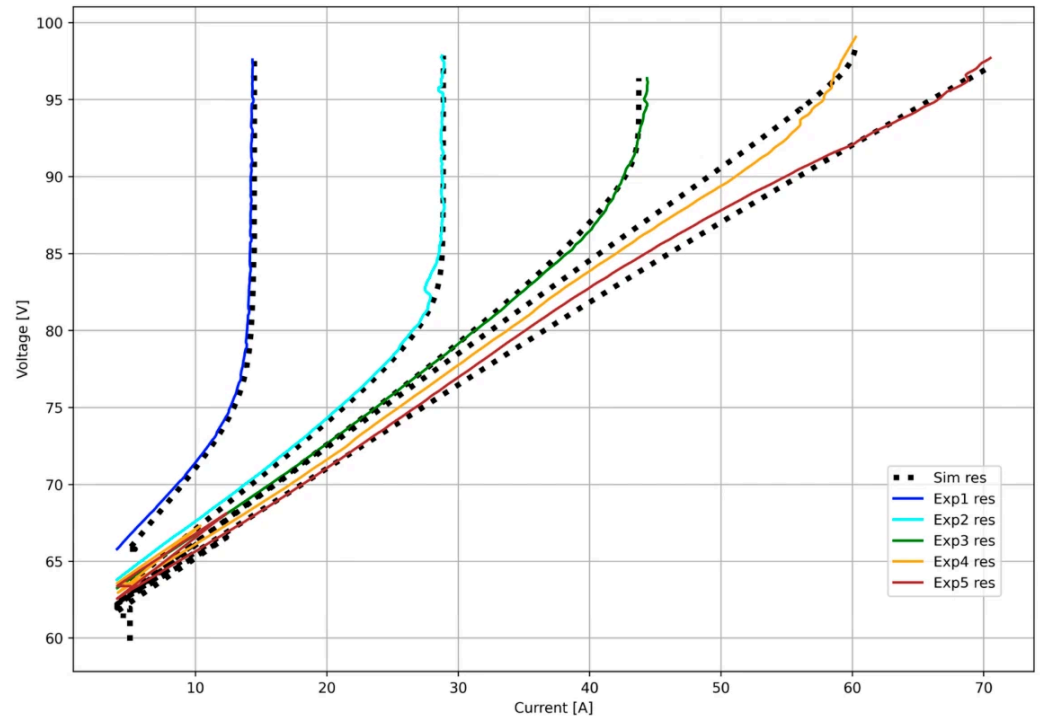
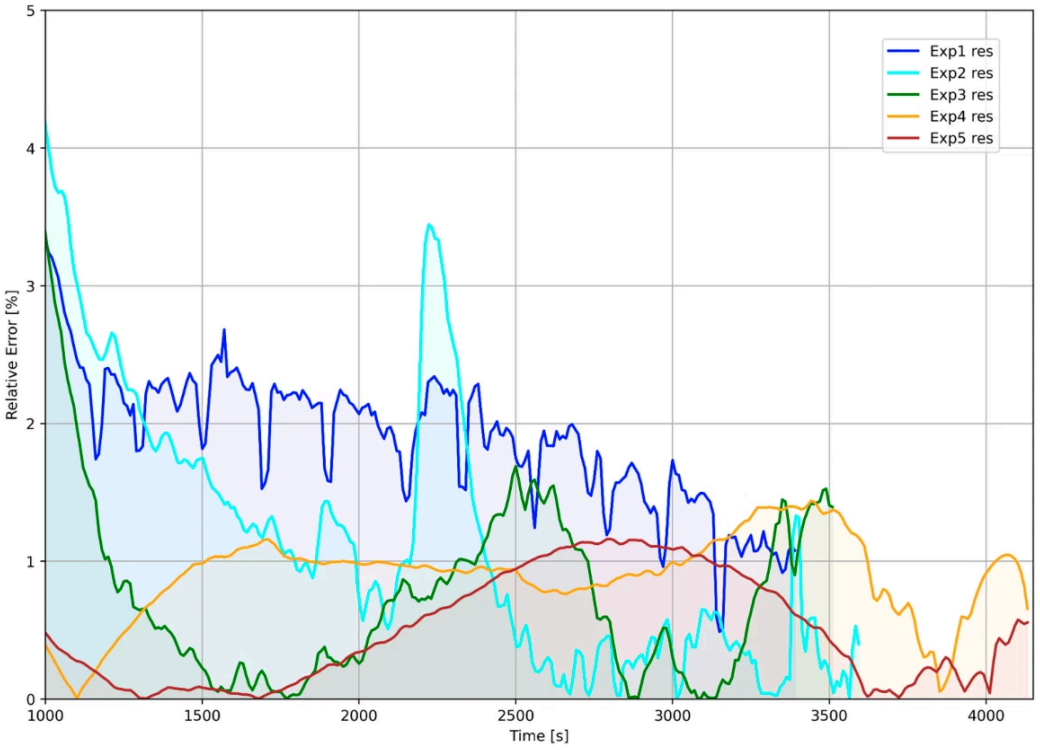


Figure 4. Experimental voltage versus steam utilisation on the 5 kW test bench, the dataset used for the calibration of the stack parameters.



(**a**)



(**b**)

Figure 5. (**a**) Validation of the polarisation curves for the five selected experiments (simulation dotted, experiments solid). (**b**) Relative error of the simulated voltage (Equation (11)) for the five selected experiments.

To set ASR_0 and E_a, data at open-circuit voltages of 1.282–1.284 V and flow rates above 1200 g/h were considered, so that ohmic losses dominate, and the Arrhenius form of Equation (6) was adopted with ASR_0 = 0.330 Ω cm^2 at 800 °C and E_a = 80.7 kJ/mol, the values fitted on the same PROMETEO campaign in [21]; the same parameter set gen-

erated all the results of Section 3. With these values, Figure 5a compares simulated and experimental polarisation curves for five experiments spanning the steam-flow range and Figure 5b the relative error,

$$\varepsilon_{rel} = 100\ \frac{V_{sim} - V_{exp}}{V_{exp}} \tag{11}$$

The error is below 3% for the blue curve and below 2% otherwise, apart from the initial points and a sensor anomaly in experiment 2. The calibrated parameters were transferred to the 25 kW configuration, which employs the same cell materials with the active area increased fourfold (80 to 320 cm^2) and 80 cells instead of the 70 of the test bench; since the ASR is normalised to area the extrapolation is well founded, while in-plane uniformity and channel pressure drops are treated as second-order until pilot data become available. The calibration subset and the five validation experiments are distinct experiments of the same campaign, so that the agreement of Figure 5 is a partial cross-validation on the same bench; an independent dataset at the pilot scale does not yet exist, the model being intended to support the pre-commissioning of the plant. The main uncertainties of the scale-up are the in-plane non-uniformity of the gas distribution and of the temperature, which the one-dimensional cell model does not resolve, and the contact resistances of the larger cells, all of which would appear as an increase in the effective ASR; the channel pressure drop is handled by the differential-pressure loop CL9. The effect of these uncertainties is bounded in Section 3.7 by repeating the reference scenario with ASR_0 varied by ±20%. The calibration of the air pre-heater E104, the dominant HEX of the network, is documented in Appendix C.

2.5. Control Architecture

Each functional zone is governed by dedicated control loops (CLs) that keep temperature, pressure, flow rate and level within their bounds, each controlled variable being paired with the manipulated variable acting most directly on it; the safety functions of the HAZOP analysis are omitted. The strategy is the second option of the test campaign [22]: the stack voltage is held at 105.6 V (1.32 V/cell, slightly above the thermoneutral voltage of about 1.29 V) by an ideal source (CL1); the steam flow is fixed per state (CL2); and the current is tracked by acting on the stack temperature through CL7 and CL8, two cascades in which an outer PI compares the measured current with the PV-derived target and outputs a temperature reference, bounded between 700 °C and the limits of the test campaign, 780 °C for the air at the stack inlet and 800 °C for the fuel heater outlet, ramped at 0.05 K/s and enforced by an inner PI on the electric heaters. Because the ASR decreases with temperature (Equation (6)), raising the inlet temperatures at constant voltage raises the current. The PI gains were tuned with the Ziegler–Nichols method, selected for its suitability to systems with slow dynamics [31], its simplicity [32] and its applicability when a precise analytical model is unavailable [33,34]. Three rules coordinate the loops with the thermal state of the stack: the references are floored at 10 K below the cell temperature of the central segment, so that the inlet gases never cool the stack faster than its own losses allow, the offset being smaller than the ΔT setpoint of CL6; the full-load steam level is held as long as either the current target or the measured current (30 s filter, 10 A hysteresis) exceeds 185 A, so that steam is never reduced ahead of the current; and the direct stack heater is controlled by a PI on the cell temperature (SH), with the fuel-side reference of CL7 as setpoint in production and 760 °C in HSB and NM, so that it covers the insulation losses when the stack is disconnected and stays idle while the electrochemical heat suffices. The ten loops are listed in Table 2.

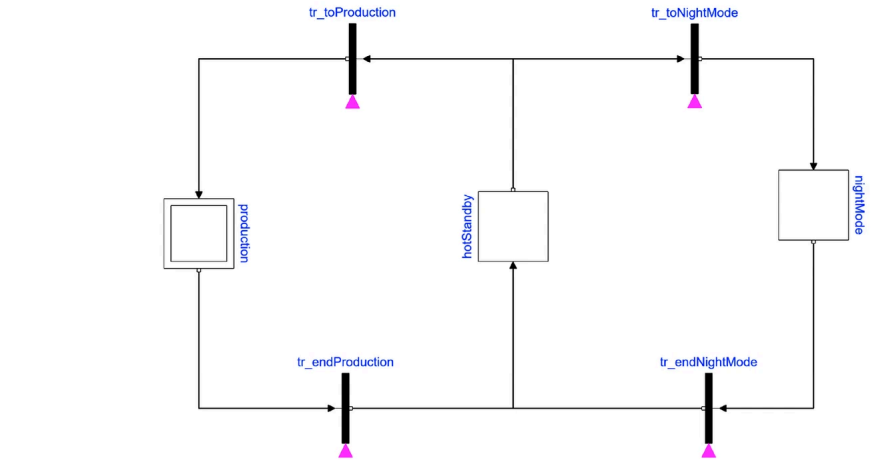
Table 2. Characteristics of the control loops of the BoP model.

Loop	Controller	Setpoint	Measurement	Manipulated Variable
CL1	Ideal source, Boolean switch	105.6 V; disconnected in HSB and NM	–	Stack voltage
CL2	PI	Steam level per state (Table 1), ramped 2×10^{-6} kg/s^2; full-load level held while target or measured current > 185 A	Steam mass flow	Steam lamination valve
CL3	PI	3 bar	Drum pressure	HTF flow to E102
CL4	ON/OFF, band 0.02 m	0.18 m	Drum level	Demineralised water pump
CL5	PI	Recirculated flow per state	Recirculated mass flow	Three-way valve; make-up H_2 and forming gas dosed by auxiliary PIs
CL6	P, production only	Air $\Delta T = 15$ K	|T_out − T_in| of the sweep air	Sweep-air flow, 0.002–0.040 kg/s, filtered ($\tau = 30$ s); frozen at the minimum in HSB and NM and while the air heater is saturated
CL7	Cascade of two PIs	Outer: current target; inner: 700–800 °C, floored at T_cell − 10 K	Stack current; fuel heater outlet temperature	Fuel heater EK101
CL8	Cascade of two PIs	As CL7, inner 700–780 °C	Stack current; air heater outlet temperature	Air heater EK102 (8 kW)
SH	PI	Fuel reference of CL7 in production; 760 °C in HSB and NM	Cell temperature, central segment	Direct stack heater
CL9	PI	Cathode–anode $\Delta p = 50$ mbar (provider requirement)	Minimum of inlet and outlet Δp	Back-pressure valve downstream of the WKO

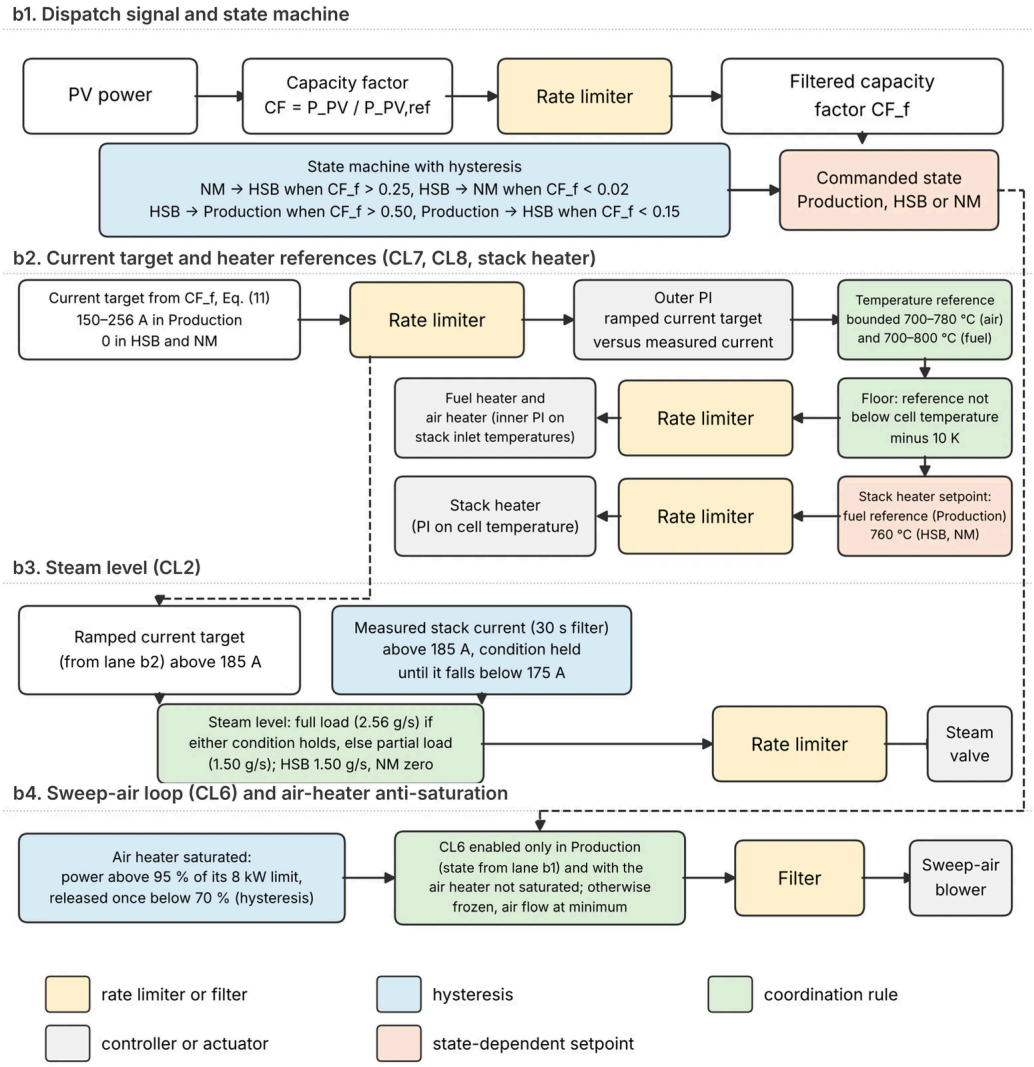
Loop	Controller	Setpoint	Measurement	Manipulated Variable
CL10	Feedforward, 1–1.35, τ = 2 s	Delivery pressure above the mixer, margin proportional to the CL5 command (≤ 150 mbar)	Mixer and suction pressures	Recirculation blower pressure ratio (Appendix G)

2.6. Supervisory State Machine and PV-Dispatched Operation

Transitions between the states are coordinated by a supervisory layer implemented with the Modelica StateGraph library (Figure 6a). The driving signal is the capacity factor CF = P_PV/P_PV,ref, with P_PV,ref = 26 kW, passed through a slew-rate limiter of 0.005 s^{-1} to obtain the filtered value CF_f, which removes the chattering of short cloud passages. Two nominal thresholds, CF = 0.10 between NM and HSB and CF = 0.30 between HSB and production, are widened into hysteresis bands: the plant leaves NM for HSB when CF_f exceeds 0.25 and returns below 0.02; it leaves HSB for production above 0.50 and returns below 0.15. The wide upper band means that a producing plant tolerates a halving of the PV power before de-energising the stack and sets the minimum depth of a cloud event able to cause a production–HSB cycle; the narrow lower band keeps the plant in HSB while any significant irradiance is available. Every shut-down or start-up passes through HSB, where steam flow and stack temperature are brought to the values of the next state. The setpoints issued by each transition are listed in Appendi x B (Table A2). CF is used here as an instantaneous per-unit PV power, close to 1 at the clear-sky peak, and differs from the annual capacity factor of PV statistics.



(**a**)



(**b**)

Figure 6. (**a**) Supervisory state machine (Modelica StateGraph) with the four signal-driven transitions. (**b**) Signal flow of the supervisory layer: dispatch signal and state machine (b1); current target, cascades, bounds, floor and stack-heater setpoint (b2); steam-level rule (b3); sweep-air enable rule and air-heater anti-saturation (b4). Dashed arrows are signals passed between lanes.

Within production the current target I_target is scaled linearly with CF_f between I_min = 150 A, assigned at the nominal threshold CF_HSB→P = 0.30, and I_max = 256 A, reached at CF_ref = 0.70 (Equation (12)); below the lower bound the target is held at 150 A, and in HSB and NM the stack is disconnected.

$$CF = \frac{P_{PV}}{P_{PV,ref}}, \qquad I_{target} = I_{min} + \left(I_{max} - I_{min}\right) \frac{CF_f - CF_{HSB \to P}}{CF_{ref} - CF_{HSB \to P}} \tag{12}$$

Figure 6b summarises the signal flow of the supervisory layer. All setpoints pass through slew-rate limiters, so that no transition reaches a loop as a step: 0.2 A/s on the current target (150 to 256 A in about 530 s, consistent with the provider-recommended ramps), 2×10^{-6} kg/s^2 on the steam setpoint, 1×10^{-7} and 1×10^{-6} kg/s^2 on the make-up and recirculation setpoints, and 0.05 K/s on all temperature references. The sweep-air loop CL6 is handled by the supervisory layer: in HSB and NM no electrochemical heat is released and a ΔT setpoint is meaningless, so the air flow is commanded to the blower minimum (0.002 kg/s) and the controller is frozen with its reference equal to the measurement; the minimum flow is retained, instead of a complete shut-down, to keep the oxygen-electrode compartment under a defined air atmosphere at a slight overpressure, to keep the air line and E104 warm for the next start-up and to hold the blower within its stable operating range, at a cost of a few watts of blower power since the air heater returns the flow at the stack temperature; the same freezing applies in production whenever the air heater is saturated (Section 3.4). The PV profile acts as a dispatch signal for a grid-connected plant and not as its sole supply: the stack absorbs 27 kW at full load against a PV peak of 27.6 kW and the auxiliaries add 3.6 kW, so that part of the demand is imported from the grid, and no electrical storage is modelled. This is consistent with the system-level study of the project [21], in which electricity is assumed to be available from the combination of PV and grid; the present work resolves which share is actually covered by the PV under a dispatch rule. The electrical accounting of Section 2.7 therefore separates the PV energy used by the plant, min(P_PV, P_el), the grid import, P_el − min(P_PV, P_el), and the unused PV power, P_PV − min(P_PV, P_el), from which the PV self-sufficiency ratio of the plant follows as the ratio of the PV energy used to the electricity demand.

2.7. Simulation Scenarios and Performance Indicators

Two consecutive days are simulated from 07:00 of the first day to 23:00 of the second (40 h). The first day uses an idealised clear-sky PV profile (hourly values, peak 27.6 kW at 12:00); the second modulates the same envelope with five events chosen to exercise the supervisory logic (Figure 7): two short morning passages (10 and 15 min at 50%), which must not trigger a state change, a 45 min overcast front at midday (10%), which drives the capacity factor below the exit threshold, one short afternoon passage and diffuse cover from 16:30 (40%). A dawn ramp from 05:00 links the two days so that the NM–HSB–production start-up is captured. The fluctuation is applied on the electrical side only, the HTF temperature being held by the thermal store; the heating-up of the plant is outside the scope, and the simulation is initialised in production at 07:00. A third scenario uses PV production derived from satellite irradiance for the site. Hourly values for Cuenca (40.07° N, 2.13° W) in 2023 were taken from the PVGIS-SARAH3 database [35] for a 30 kWp crystalline-silicon array at the optimum tilt of 38° facing south with 14% system losses, centred on the half hour, converted to local time and scaled by 1.027, so that the clear-sky peak of the year matches the 27.6 kW of the reference profile. Of the year, 2 and 3 July were selected as the consecutive pair in which the hourly profile crosses both hysteresis thresholds most often within long production periods. The simu-

lation covers 35.5 h from 11:00 local time on 2 July, when CF = 0.52, so that the initialisation in production is retained. The hourly resolution smooths fluctuations shorter than one hour, and the synthetic day is therefore kept as the more demanding test of the hysteresis logic. To assess the effect of the field size, the same two days are repeated with the PV power scaled by 2 and 3, P_PV,ref being kept at 26 kW so that the thresholds and the current target refer to the same absolute PV power.

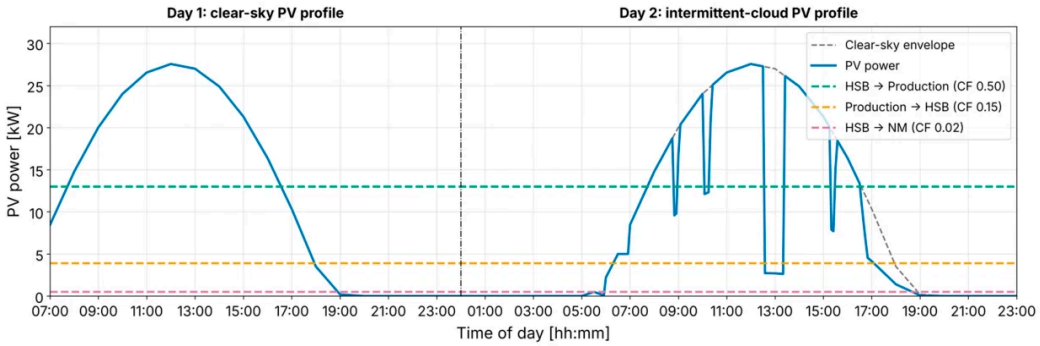


Figure 7. PV power profile over the two simulated days: idealised clear-sky day followed by the synthetic intermittent-cloud day. Dashed lines mark the state-machine thresholds expressed in PV power.

The indicators are the hydrogen production, the total electrical power, the specific electricity consumption CS and the PV, and grid and unused-PV shares of the electricity demand defined in Section 2.6. CS is the electricity demand of the plant per kilogram of hydrogen regardless of the source of the electricity, and does not include the solar-thermal heat supplied to the steam generator by the HTF loop; it is therefore a demand metric of the plant and not a PV-to-hydrogen conversion efficiency. No electrical or thermal storage is modelled, so that storage losses do not enter the balance. The electrical power collects the stack, the fuel, air and stack heaters, the chiller duty converted with a coefficient of performance of 3, the recirculation blower (compression work divided by the motor efficiency η_m, Appendix G) and the sweep-air blower:

$$P_{el} = P_{stack} + P_{fuelheater} + P_{airheater} + P_{stackheater} + \frac{Q_{chiller}}{COP} + \frac{P_{c,rec}}{\eta_m} + P_{blower} \quad (13)$$

$$CS = \frac{P_{el}}{\dot{m}_{H_2}}, \qquad CS_{day} = \frac{\int P_{el}\, dt}{\int \dot{m}_{H_2}\, dt} \quad (14)$$

$$P_{blower} = \frac{\dot{m}_{air}\, \Delta p_{air}}{\rho_{air}\, \eta_{blower}\, \eta_{motor}} \quad (15)$$

The instantaneous CS is reported only while hydrogen is produced; the daily value CS_day is the ratio of the integrals over the whole day, standby and night included. The sweep-air blower power uses the pressure drop of the modelled air network, an air density of 1.17 kg/m^3 and efficiencies of 0.55 and 0.90, and is a lower bound.

2.8. Use of Generative AI Tools

Claude (Anthropic; Claude Sonnet 5) was used during the preparation of this work for the language editing of the text, for the generation of the Python 3.14.5 (Python Software Foundation, Wilmington, DE, USA) scripts that plot the result figures (Figures

7–16) from the simulation outputs, and for the drafting of the explanatory diagram of Figure 6b from the description of the supervisory logic given by the authors. All outputs of the tool were reviewed, verified against the simulation results and edited by the authors.

3. Results and Discussion

3.1. Clear-Sky Day and Control Loop Behaviour

Figure 8 summarises the two days at 105.6 V. On the clear-sky day the plant is in production from 07:00, when the initial capacity factor of 0.33 exceeds the entry threshold, until 17:56, in HSB until 18:54 and in NM afterwards. The current follows the PV signal with the 0.2 A/s ramp, on the 256 A plateau from 08:39 to 15:37; hydrogen production peaks at 0.77 kg/h for a daily total of 7.85 kg. The inlet temperatures on both sides are set by the cascades: 774 °C at full load, 706 °C at the end of the evening ramp-down, when the references rest on their 700 °C bound, and 760 °C in HSB and NM; the cell temperature follows within a few kelvin. The air panels show the thermal balance of the strategy: at 1.32 V/cell the electrochemical heat at 256 A, about 0.8 kW, matches the insulation losses (860 W), the measured air ΔT settles at 12.7 K, below the 15 K setpoint, and CL6 keeps the air flow at the blower minimum throughout; the current is tracked through the inlet temperatures alone.

On the plateau the stack absorbs 27.0 kW and the auxiliaries 3.6 kW: 2.6 kW in the fuel heater, which raises the steam from 133 °C beyond what E103 recovers, 0.8 kW in the chiller (2.4 kW of cooling at a COP of 3) and 0.2 kW in the air heater; the stack heater is idle on the plateau and delivers up to 2.3 kW for a few minutes at start-up and re-entries. The sweep-air blower requires 2–21 W and contributes less than 0.01 kWh/kg to CS. The instantaneous CS is 39.8 kWh/kg on the plateau and 41 kWh/kg at the end of the ramp-down. Over the clear-sky day the plant consumes 346 kWh for 7.85 kg, a daily CS of 44.1 kWh/kg, of which the night accounts for 28 kWh at 2.4 kW (0.8 kW fuel heater, 0.75 kW stack heater, 0.45 kW air heater, 0.3 kW chiller) against 840 W of insulation losses, the balance being carried away by the night-mode gas flows; the value is consistent with the 38.7 kWh/kg at design point of the 100 kW module [21], the difference being due to ramps, standby and auxiliaries.

Over the two days the PV energy available is 411 kWh against a plant electricity demand of 616 kWh (Figure 9): 403 kWh is supplied by the PV, 214 kWh is imported from the grid and 8 kWh of PV remains unused, so that the self-sufficiency ratio is 65%, 64% on the clear-sky day and 66% on the intermittent-cloud day. The grid import is concentrated in production, 172 kWh over 19.5 h, where the plateau demand of 30.6 kW exceeds the PV peak, and in night mode, 37 kWh over 16.4 h, where the 2.4 kW of heaters and the chiller is imported entirely, a standby demand of the same order, per unit of stack power, as the 6.4 and 8.0 kW reported for the hot standby and night modes of the 100 kW module [21]; the unused PV, 6 kWh, occurs in HSB on the second day, while the plant waits for the capacity factor to exceed the re-entry threshold. The 44 kWh/kg is thus the demand of the plant per kilogram of hydrogen, of which about 29 kWh/kg is supplied by the PV and 15 kWh/kg by the grid under the present dispatch rule.

Figure 10 shows the remaining loops on the clear-sky day. CL2 tracks the two steam levels with valve openings of 73 and 91% and closes the valve at the transition to NM; CL3 holds the drum pressure within 5 mbar of 3 bar with an HTF flow of 0.04–0.10 kg/s; CL4 produces the sawtooth of the drum level between 0.17 and 0.19 m with a period of about 160 min. CL5 keeps the recirculated flow at 0.03 g/s in production and 0.63 g/s in NM, the make-up loops dose 0.02 g/s of hydrogen in HSB and 0.07 g/s of forming gas in NM, and the recirculation blower runs at pressure ratios of 1.02–1.20 with 9–54 W elec-

trical power. CL9 holds the 50 mbar minimum differential with the back-pressure valve at 13% in production and 17% in NM, the transient minimum of 21 mbar occurring at the entry into HSB. The stack heater loop is idle while the cascades hold the stack at 774 °C, delivers a 2.3 kW pulse at the transition to HSB, when the reference returns to 760 °C from 713 °C, and settles at 0.75 kW in NM.

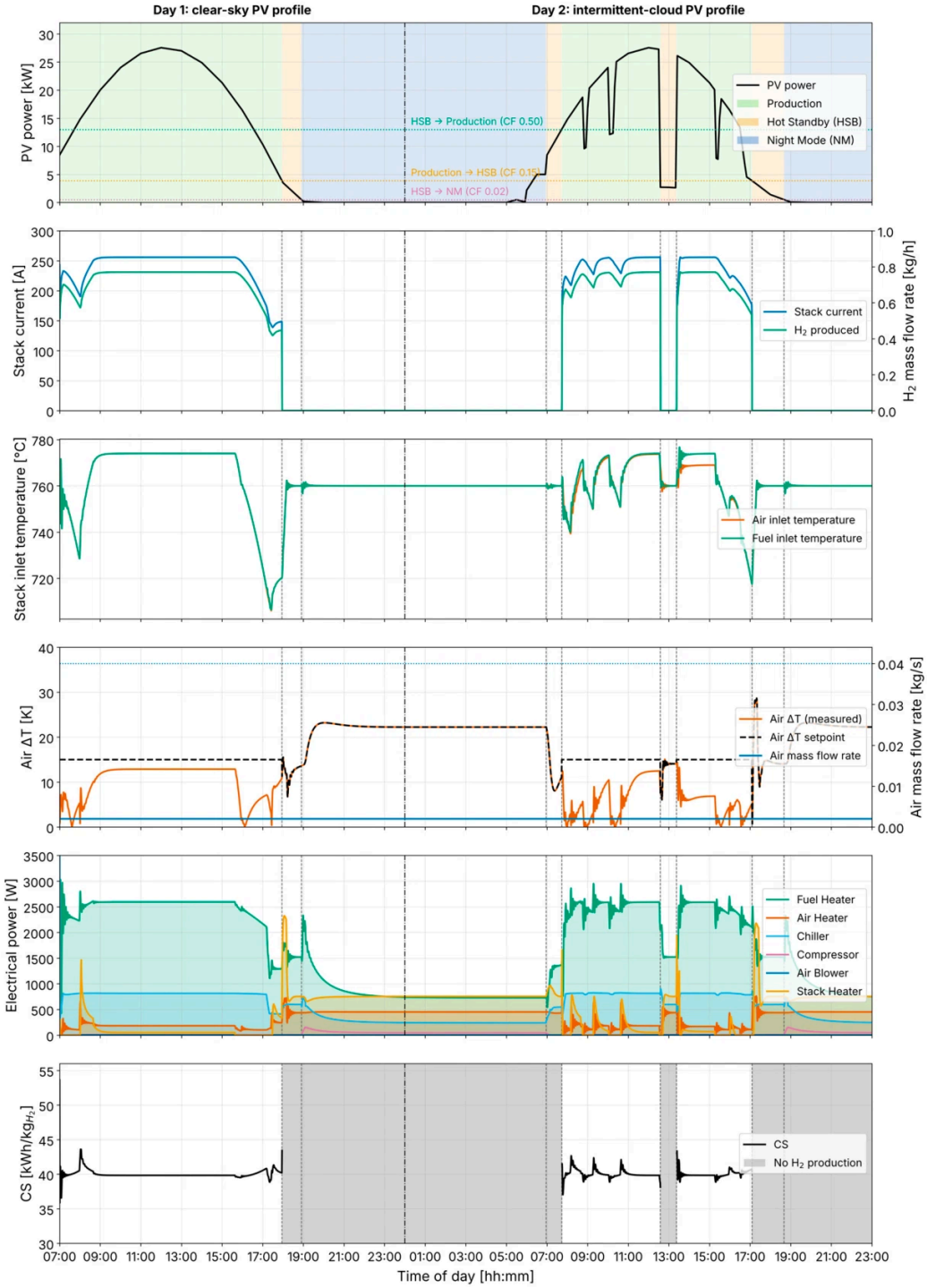


Figure 8. Two-day simulation at 105.6 V. From top: PV power with supervisory state and thresholds; stack current and hydrogen production; stack inlet temperatures; sweep-air ΔT and air flow (CL6); electrical power of the auxiliaries; specific consumption CS (grey: no hydrogen production).

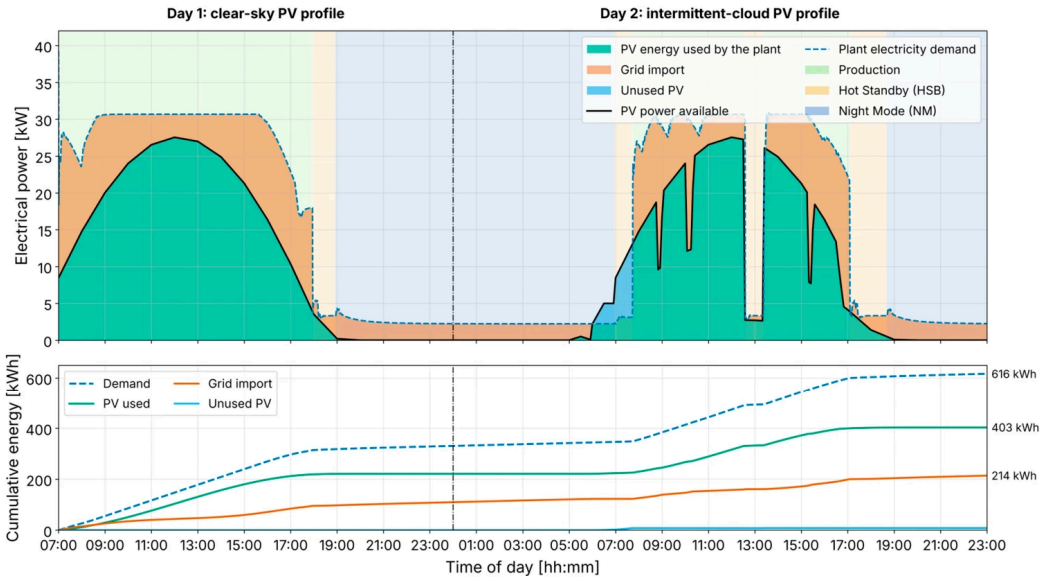


Figure 9. Electrical balance of the plant over the two days at 105.6 V: PV power available, plant electricity demand and its coverage by the PV, grid import and unused PV (**top**); cumulative energies (**bottom**).

Figure 11 shows the cascades CL7 and CL8 over the two days. On the clear-sky day the current is within 3 A of its target on average in production and lags by up to 20 A during the evening ramp-down, when the references fall at 0.05 K/s and, having floored at 10 K below the cell temperature, can only follow the natural cooling of the stack. The references on both sides coincide, from 774 to 700 °C, and are followed by the inner loops within 4 °C; the fuel heater delivers 2.6 kW and the air heater 0.2 kW at full load, and neither approaches its limit. At the start of the simulation the stack, initialised at 760 °C, delivers 243 A against a target of 150 A: the cascades lower the references to 700 °C within 20 min and the current meets the rising target at 07:41 without overshoot. Outside production the references are replaced by the 760 °C maintenance value and the outer-loop error is nulled, so that no wind-up occurs. On the intermittent day, the cloud passages, which lower the target to 169 A, are followed with deviations of up to 30 A, because the two ramp limits are not commensurate: a change of 87 A takes 7 min, and the corresponding 35 °C takes 12 min. At the re-entry at 13:22 the current reaches the target at 13:31 without overshoot, the stack heater contributing 2.2 kW for the first minutes; with a stack of negligible thermal capacity the same re-entry produces an overshoot beyond 300 A. The two outer loops act on the same error with independent integrators and coincide within 2 °C here; a single outer loop feeding both references would remove the ambiguity by construction.

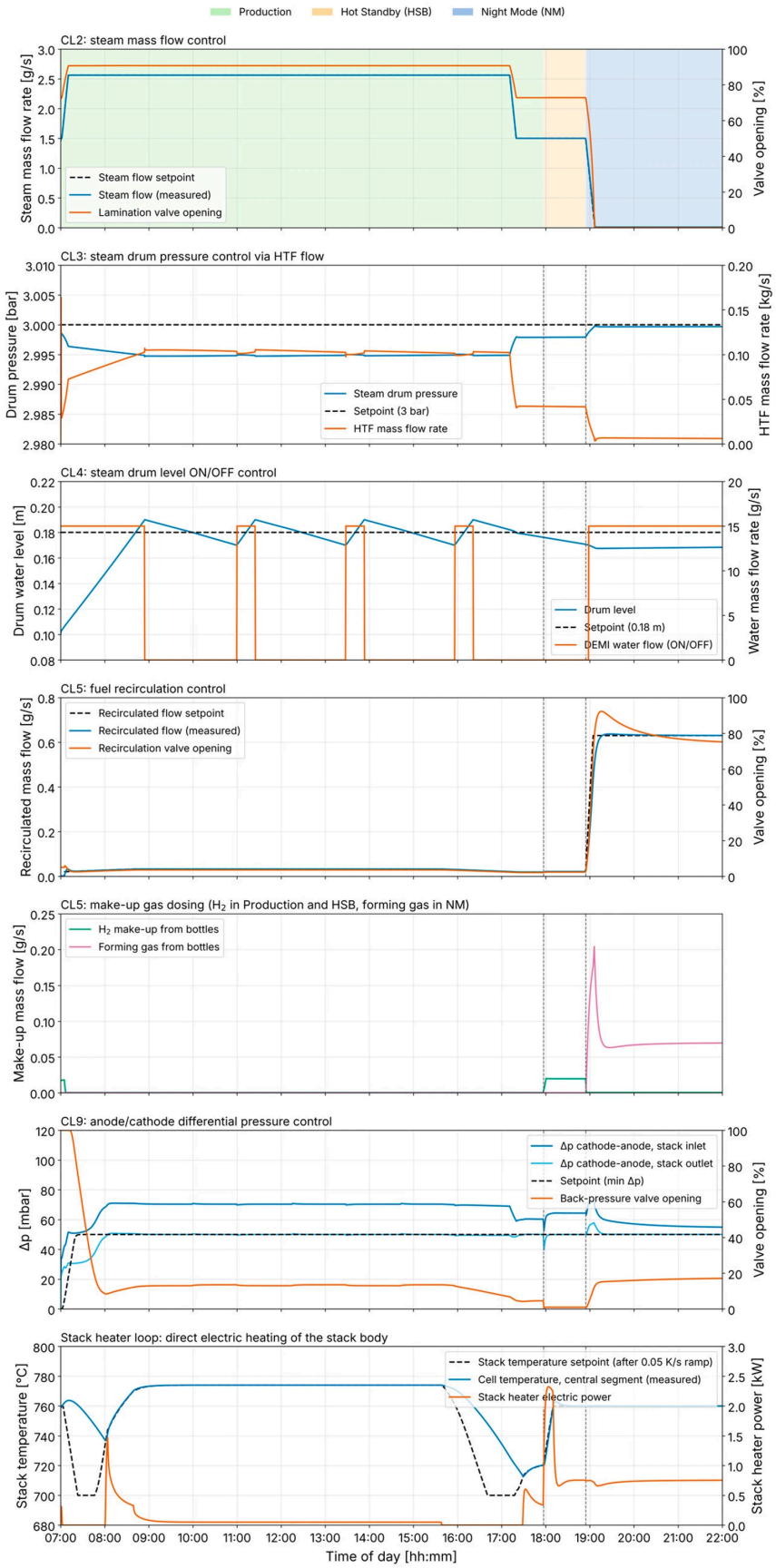


Figure 10. Control loops CL2, CL3, CL4, CL5 (recirculation and make-up dosing), CL9 and the stack heater loop on the clear-sky day at 105.6 V (setpoints dashed, manipulated variables in red on the right axes).

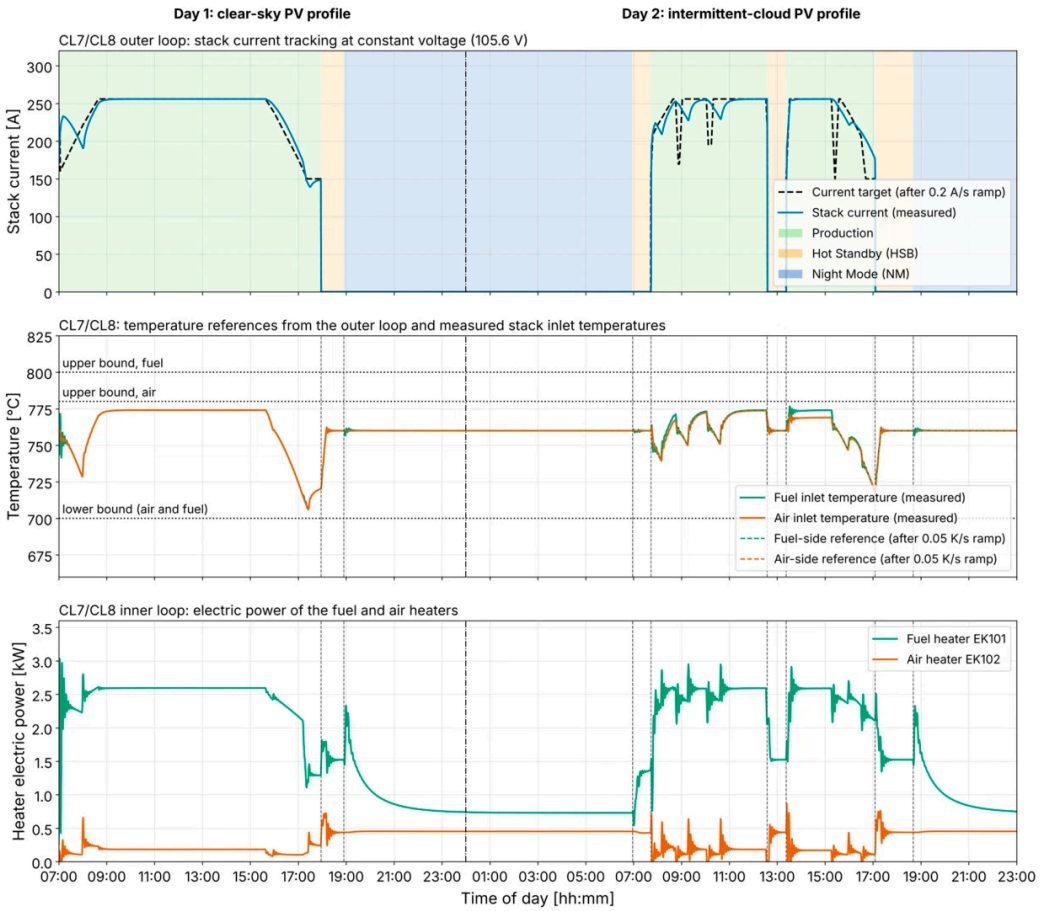


Figure 11. Current-tracking cascades CL7 and CL8 over the two days at 105.6 V. From top: stack current and its ramped target; temperature references after the 0.05 K/s ramp (dashed) and measured inlet temperatures, with the 700 °C lower bound and the 780 °C (air) and 800 °C (fuel) upper bounds; electric power of the fuel and air heaters.

3.2. Sensitivity to the Stack Voltage

At constant voltage the thermal balance of the stack depends on the voltage directly: at the thermoneutral voltage, ΔH_r/2F, about 1.29 V/cell between 750 and 800 °C for the water-splitting reaction, the electrochemical heat is zero; above it the stack is exothermic and below it endothermic. The stack as a whole is in heat balance at a slightly higher voltage, where the exothermic heat equals the insulation losses: with the present insulation losses of 0.84–0.86 kW, between 760 and 775 °C, this heat-balance point is 1.32 V/cell at 256 A and moves up as the current decreases, 1.36 V/cell at 150 A, so that the stack heater or the inlet temperatures must cover the deficit at part load. The 105.6 V (1.32 V/cell) of the test campaign [22] was therefore tested against 102.4 and 104.0 V (1.28 and 1.30 V/cell) and 108.0 and 110.4 V (1.35 and 1.38 V/cell) on the two-day scenario (Figure 12 and Table 3). The three lower voltages complete the two days with practically unchanged hydrogen production and consumption, 13.91–14.07 kg and 43.8–44.0 kWh/kg, because the cascades reach the supervisory target at every voltage by adjusting the stack temperature. What changes is the thermal operating point. At 105.6 V the stack runs at 774 °C with the stack heater idle; at 104.0 V the cascades raise it to 780 °C and the stack heater supplies 0.5 kW on the plateau; at 102.4 V the air-side reference sits at its 780 °C bound for 7.4 h, the fuel side compensates at 790 °C, the cell temperature reaches 786–790 °C, above the 780 °C upper limit of the nominal range [22], and the stack heater supplies 1.0 kW on the plateau and 34 kWh over the two days against 18 kWh at 105.6 V.

The lower end of the feasible window is thus set by the stack temperature limit and lies between 1.28 and 1.30 V/cell.

Table 3. Sensitivity to the stack voltage over the two days (ΔT = 15 K, steam levels of Table 1); the runs at 108.0 and 110.4 V do not complete the scenario.

Stack Voltage (V)	Cell Voltage (V)	H_2 Day 1/Day 2 (kg)	Electrical Energy (kWh)	CS_Day Day 1/Day 2 (kWh/kg)	Cell Temperature, Min/Max (°C)	Air Reference at 780 °C Bound (h)	Stack Heater Energy (kWh)	Fuel/Air Heater Energy (kWh)
102.4	1.28	7.77/6.14	612	44.2/43.7	729/790	7.4	33.7	68.6/12.6
104.0	1.30	7.77/6.15	612	44.2/43.6	716/783	0.0	25.5	68.6/12.9
105.6	1.32	7.85/6.22	616	44.1/43.5	713/776	0.0	17.9	68.4/12.7

The two higher voltages fail by the same mechanism. At 108.0 V the current delivered by the stack at 760 °C exceeds the target from the first minutes and the cascades bring the references to their 700 °C bound within 20 min; the temperature lever is then exhausted while the current is still above the target, and the current settles at the value that the steam supply can sustain at 100% utilisation, 201 A on the partial-load level and 343 A on the full-load level. The last segments of the channel run dry, the Nernst voltage of Equation (2) diverges as the steam partial pressure vanishes, and the heat released at 1.35 V/cell and 343 A exceeds what the sweep air can remove at the blower maximum: the cell temperature rises without bound, 830 °C at 08:00 and above 1000 °C by 09:50, until the steam-side properties leave their validity range. At 110.4 V the anode channel dries within the first hour. Constant-voltage operation is therefore feasible only within a narrow window, about 1.30–1.33 V/cell with the present steam levels, and above it the strategy requires a protection it does not contain, either a current limiter acting on the voltage, as in the first option of the test campaign, or a steam feedforward on the measured current. The steam-level rule of Section 2.5 prevents steam starvation during the evening ramp-down but cannot cover a voltage at which the current exceeds the full-load steam supply. The sweep-air setpoint of 15 K, selected through a preliminary sensitivity over 5–25 K with a stack of negligible thermal capacity, is retained: with 25 kJ/K the loop stays at the blower minimum at all feasible voltages, so that the setpoint acts as an upper limit on the stack exothermicity.

The two bounds of the window respond differently to the operating conditions. The upper bound is set by the current that the steam supply can sustain at full utilisation,

$$I_{steam} = \frac{2F\,\dot{m}_{steam}}{n_{cell}\,MM_{H_2O}} \tag{16}$$

201 A and 343 A for the two steam levels of Table 1, so that it moves in proportion to the steam flow (Figure 13a): a target above 343 A at 1.35 V/cell would require a third steam level, whereas a lower full-load level would bring the limit into the present target range. The lower bound is set by the heat balance of the stack, which is reached when the exothermic heat covers the insulation losses,

$$V_{hb} = V_{tn} + \frac{UA\ (T_{cell} - T_{amb})}{n_{cell}\ I} \tag{17}$$

where V_tn is the thermoneutral voltage and UA = 1.15 W/K the conductance of the insulation; V_hb is 1.32–1.33 V/cell at 256 A and 1.36 V/cell at 150 A, and below it the heaters must supply the deficit, which drives the cell towards the 780 °C limit at 1.28

V/cell. The ambient temperature enters only through the insulation losses: a change of 20 K moves V_hb by 0.001 V/cell (Figure 13b) and is therefore immaterial, whereas a doubling of the insulation losses, as for a degraded insulation, shifts it by 0.04 V/cell at 256 A. The stack thermal capacity moves neither bound, as shown in Section 3.3, because it affects only the lag with which the current follows its target. The window of about 1.30–1.33 V/cell therefore holds for the present steam levels of 1.50 and 2.56 g/s, the present insulation, an ambient temperature of 25 °C and a thermal capacity of 25 kJ/K, and should be re-evaluated with Equations (16) and (17) whenever these are changed.

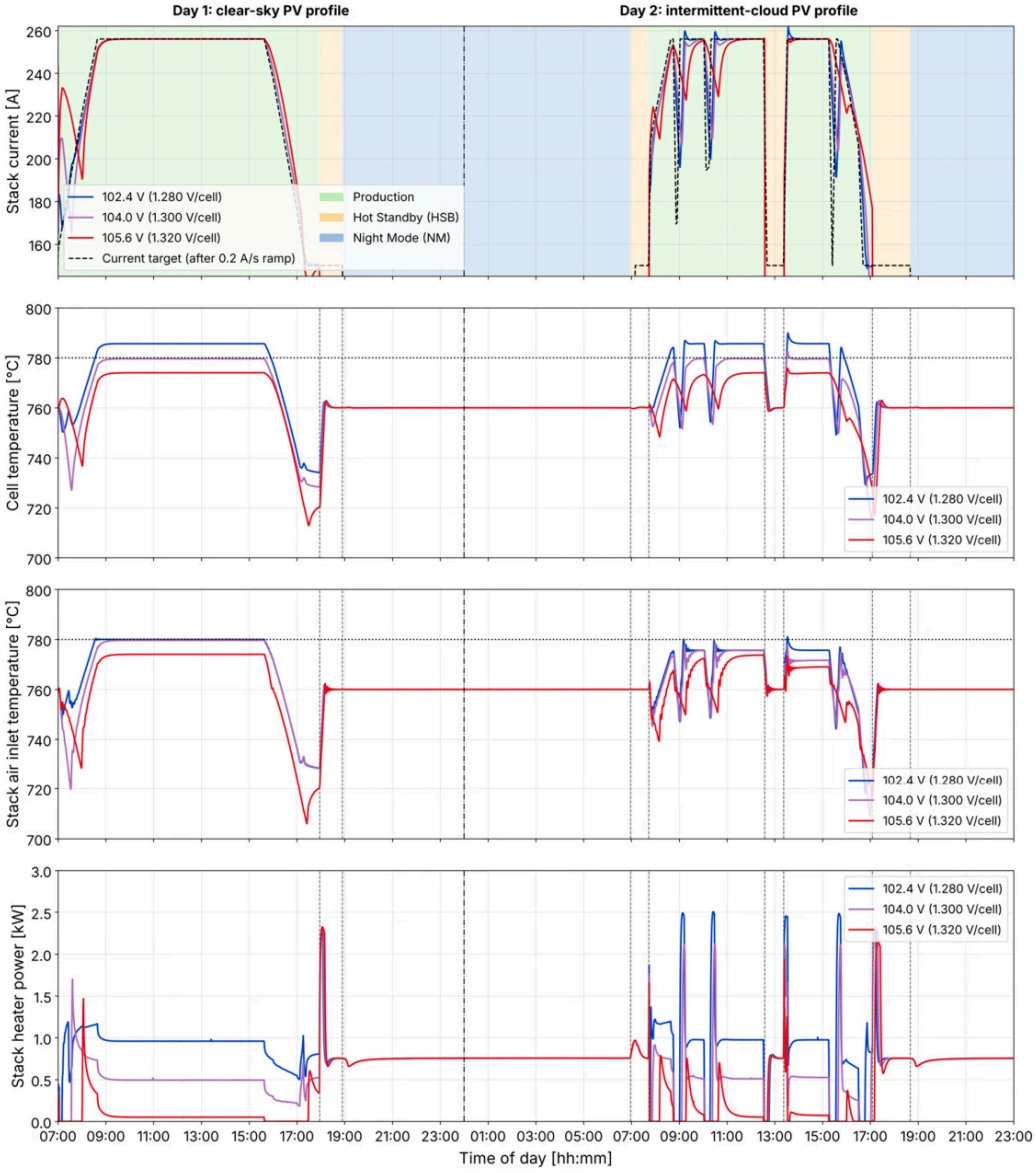


Figure 12. Sensitivity to the stack voltage (102.4, 104.0 and 105.6 V, i.e., 1.28, 1.30 and 1.32 V/cell) over the two days: stack current with its target; cell temperature of the central segment, with the 780 °C upper limit of the nominal stack range; stack air inlet temperature, with the 780 °C bound of the air-side reference; stack heater power. The runs at 108.0 and 110.4 V terminate on the first morning.

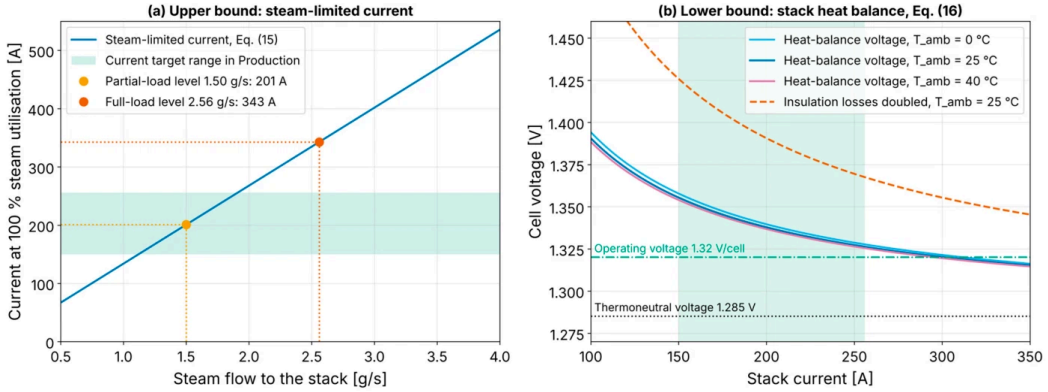


Figure 13. Trends of the feasible voltage window: (**a**) steam-limited current as a function of the steam flow to the stack (Equation (16)) with the two steam levels of Table 1 and the current target range; (**b**) heat-balance voltage of the stack as a function of the current (Equation (17)) for ambient temperatures of 0, 25 and 40 °C and for doubled insulation losses, with the thermoneutral and operating voltages.

3.3. Sensitivity to the Stack Thermal Capacity

The stack thermal capacity of 25 kJ/K is a literature-based estimate (Appendix D) and sets the pace at which the temperature-tracking strategy can act. Its influence was assessed at 105.6 V with 6.25, 12.5, 25 and 50 kJ/K (Figure 14 and Table 4). The strategy completes the two days at every value, with the sweep-air loop at the blower minimum and the air heater below 1 kW, and the specific consumption is unchanged, 43.7–43.9 kWh/kg. The capacity changes the lag between the current and its target: on the first morning the current meets the target at 07:23 with 6.25 kJ/K and at 07:56 with 50 kJ/K, and the cloud passages are followed with deviations of 20 and 45 A. The evening ramp-down is the most sensitive event, because the stack can only cool at the rate of its insulation losses once the references have reached their floor: with 6.25 and 12.5 kJ/K the current follows within 7 A, with 25 kJ/K it lags by up to 15 A, and with 50 kJ/K the stack is still at 195 A when the target reaches the 150 A floor and the supervisory layer disconnects it. The hydrogen output rises accordingly, from 13.94 to 14.39 kg, and the stack heater pulses at the transitions grow from 2.0 to 3.8 kW. A stack twice as heavy as assumed here would still be operated safely, but its current could not be brought to the floor at the end of the day by the temperature alone, and the current limiter recommended in Section 3.2 would be needed at the ramp-down as well.

Table 4. Sensitivity to the stack thermal capacity at 105.6 V over the two days.

Stack Thermal Capacity (kJ/K)	H_2 Day 1/Day 2 (kg)	Electrical Energy (kWh)	CS_Day Day 1/Day 2 (kWh/kg)	Cell Temperature, Min/Max (°C)	Mean |I − I_Target| in Production (A)	Current at Disconnection, Day 1 (A)	Stack Heater Energy/Peak (kWh/kW)
6.25	7.79/6.15	611	44.1/43.5	717/775	6	150	17.5/2.0
12.5	7.81/6.18	613	44.1/43.5	712/776	7	150	17.7/1.9
25	7.85/6.22	616	44.1/43.5	713/776	9	149	17.9/2.3
50	8.10/6.29	629	43.9/43.4	729/776	14	195	17.8/3.8

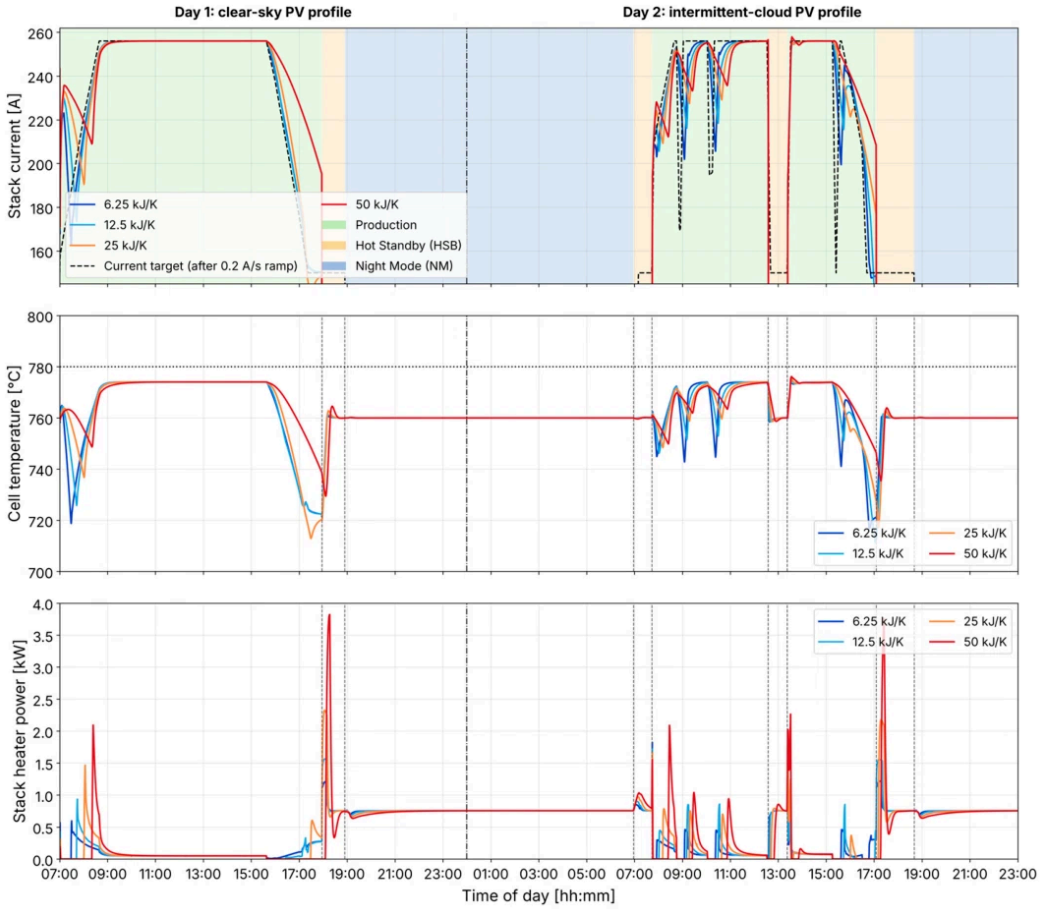


Figure 14. Sensitivity to the stack thermal capacity (6.25, 12.5, 25 and 50 kJ/K) at 105.6 V over the two days: stack current with its target; cell temperature of the central segment; stack heater power.

3.4. Sweep-Air Loop Outside Production and Its Coordination with the Cascades

Two results on the sweep-air loop emerged from configurations that failed. The first is the requirement to disable CL6 in HSB and NM, absent from the original control specification. With the stack disconnected the air leaves the stack colder than it enters, the measured ΔT exceeds any setpoint and CL6 raises the air flow towards the blower maximum: with the original 0.020 kg/s blower the flow saturates at the entry into HSB and remains saturated all night; with the 0.040 kg/s blower the saturation moves to the heaters, the air heater sitting at its 8 kW limit while the stack inlet falls to 634 °C and the night-time heating demand reaches 28 kW. These figures were obtained with the thermal capacity of the original stack model, but the night-time saturation is a steady-state condition independent of the inertia. Holding the air flow at the minimum outside production keeps the stack at 760 °C with 2.4 kW: the sweep-air loop is a production-state controller whose activation must be a supervisory decision.

The second result appeared when the stack thermal capacity was corrected from the per-cell value of the original model (312 J/K for the lumped stack) to 25 kJ/K, before the floor on the references and the stack heater were introduced. With a stack that no longer follows its inlet temperatures within seconds, the references fell below the stack temperature during the evening ramp-down; the sweep air entered the stack colder than the cells, the measured ΔT exceeded the setpoint, CL6 opened the air flow to the blower maximum, the air heater saturated at 8 kW, and the stack, disconnected shortly after, lost the 700–830 W of its insulation losses that neither the gas flows nor the saturated heater could return: it cooled below 700 °C during the first night and the plant did not recover.

The three rules of Section 2.5 and Figure 6b remove the mechanism, and with them the two days are completed with the air flow at the minimum and the air heater below 1.4 kW at every voltage and thermal capacity of Sections 3.2 and 3.3. The lesson holds for any temperature-tracking strategy: the loops that heat the stack and the loop that cools it must be coordinated with the stack temperature itself; otherwise, they work against each other through the stack thermal inertia.

3.5. Intermittent-Cloud Day and Supervisory Behaviour

The second day of Figure 8 tests the supervisory logic. The start-up follows the intended sequence, NM to HSB at 06:57 and HSB to production at 07:43. The short cloud passages reduce the target to 169 A without leaving production, the filter and the hysteresis band absorbing them as intended. The midday front drives the capacity factor below 0.15: the plant enters HSB at 12:34, after the current has ramped down to 150 A, and returns to production at 13:22, an excursion of 48 min; the diffuse afternoon cover brings the exit from production forward to 17:05 and the entry into NM to 18:40. Hydrogen production is 6.22 kg against 7.85 kg on the clear-sky day, for 185 against 225 kWh of PV energy, and the daily CS of 43.5 kWh/kg is practically equal. The steam, pressure, level and recirculation loops behave as on the clear-sky day at every transition. The two re-entries (07:43 and 13:22) are the most demanding events: the stack, connected at 105.6 V while at 760 °C, delivers at once about 200 A against a target restarting from 150 A; the cascades lower the references towards 700 °C, the stack heater delivers a 2.2 kW pulse when the references turn upwards again, and the current meets the target within 9 min without overshoot. The air ΔT, negative in HSB, returns below the setpoint within minutes, so that CL6 stays at the minimum and the air heater below 0.8 kW. The cell temperature stays between 728 and 776 °C, within the 680–780 °C window, with no oscillatory behaviour. These results complement the steady-state optimisation of [21], which identified the anode air flow as the parameter governing thermal management: dynamically, the air path is the binding constraint during the transitions and outside production, where the supervision of the loop decides whether the plant can be held hot at an acceptable cost, the blower size being of secondary importance.

3.6. Two Days with Satellite-Derived PV Production

Figure 15 shows the scenario built on the PVGIS production of 2 and 3 July 2023, and Table 5 compares its indicators with those of the reference scenario. The state machine performed eight transitions in 35.5 h, in the sequence expected from the hysteresis bands. On the first day the plant stayed in production until 19:27 and entered night mode at 21:12. On the second day it left night mode at 09:44, entered production at 10:53, returned to hot standby from 16:18 to 17:17, when the PV fell from 15 to 1.3 kW, produced again until 18:21 and entered night mode at 21:12. The drops to 6.7 kW at 16:30 on the first day and to 9.9 kW at 13:30 on the second remained inside the band and were absorbed by load modulation without a change of state.

Table 5. Indicators of the scenario with satellite-derived PV production (2–3 July 2023, 35.5 h) for the reference field and for the PV power scaled by 2 and 3, compared with the reference scenario (40 h) at 105.6 V.

Indicator	PVGIS ×1	PVGIS ×2	PVGIS ×3	Reference, Figure 8
State transitions (production → HSB/HSB →	8 (3/2)	8 (3/2)	6 (2/1)	8 (3/2)

Indicator	PVGIS ×1	PVGIS ×2	PVGIS ×3	Reference, Figure 8
production)				
Time in production/HSB/NM (h)	14.9/6.7/13.8	17.7/5.1/12.7	20.9/2.5/12.1	19.5/4.1/16.4
Time at 256 A (h)	2.6	11.3	14.0	9.8
Hydrogen, first/second day (kg)	5.59/4.24	6.95/6.28	7.30/8.16	7.85/6.22
Hydrogen, total/from current target (kg)	9.82/9.64 (+1.9%)	13.23/12.90 (+2.6%)	15.46/14.97 (+3.2%)	14.07/13.90 (+1.2%)
Mean |I − I_target| in production (A)	9.0	10.2	11.1	7.6
Central cell segment, min/max (°C)	714/774	712/774	713/774	713/776
Hottest segment, max (°C)/excursions above 780 °C/time above 780 °C (h)	781.2/2/3.1	781.1/4/12.3	781.1/3/14.5	783.2/4/10.9
Air reference at the 780 °C bound (min)	1.7	1.7	0.7	2.0
Air heater saturated (h)/maximum air flow (kg/s)	0/0.0021	0/0.0060	0/0.0074	0/0.0020
PV available/used/unused (kWh)	247/233/14	494/445/49	741/529/211	411/403/8
Electricity demand/grid import (kWh)	452/219	576/131	655/126	616/214
PV self-sufficiency (%)	51.5	77.3	80.8	65.3
Specific electricity demand (kWh/kg)	46.0	43.5	42.4	43.8
Stack heater energy (kWh)/peak (kW)	18.3/2.33	15.1/2.32	13.1/2.34	17.9/2.33

Hydrogen production was 5.59 kg on the first day and 4.24 kg on the second, 9.82 kg in total and 1.9% more than the 9.64 kg corresponding to the current target, because the current lags above a falling target. The mean deviation between current and target in production was 9 A, and the current stayed within 10 A of the target for 72% of the production time. The largest deviations arose in the first minutes after each entry into production, while the load was connected through its 60 s transition, and at 16:00 on the second day, when the target fell to 150 A faster than the stack could cool and the current lagged by up to 53 A, the mechanism observed at the evening ramp-down in Sections 3.1 and 3.3.

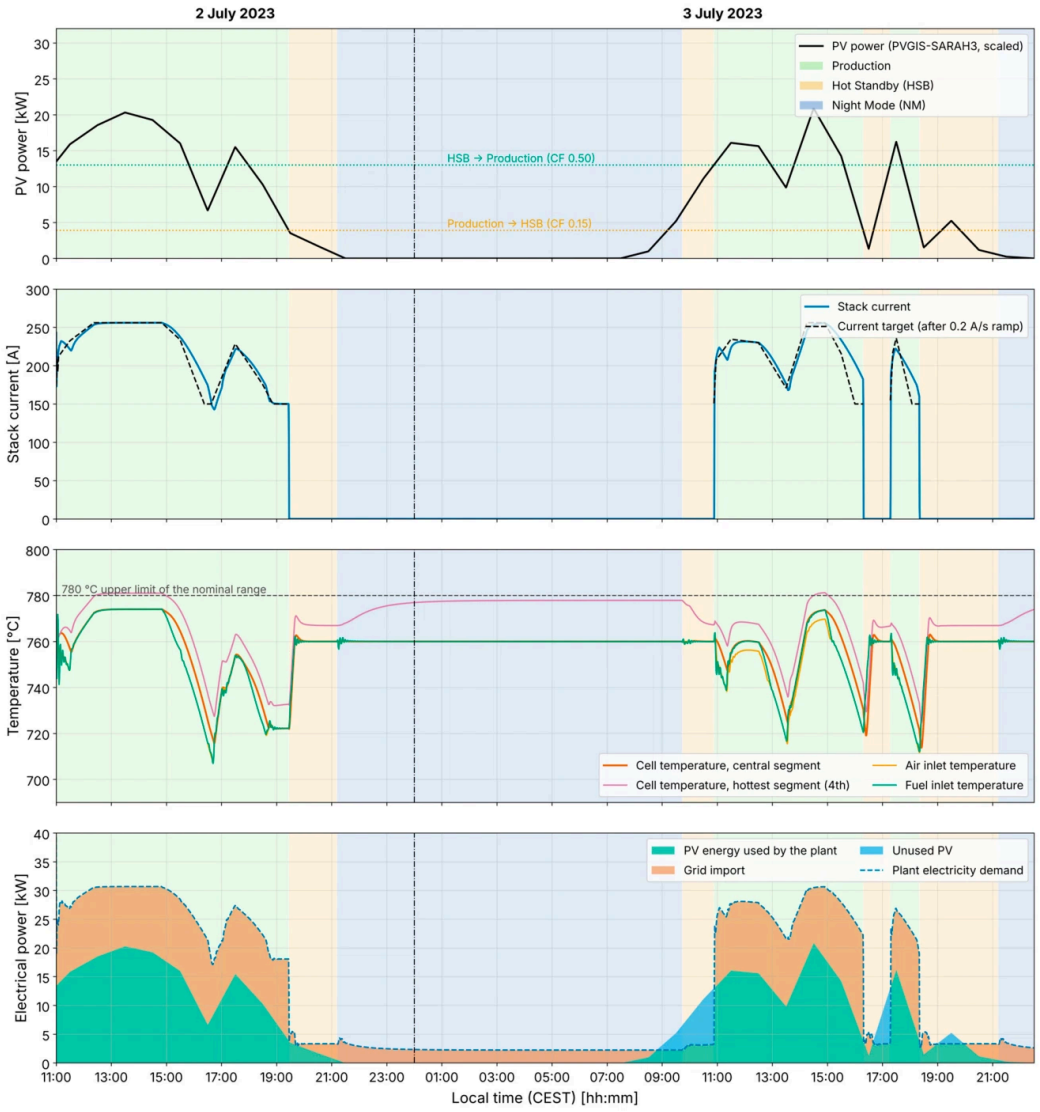


Figure 15. Scenario with satellite-derived PV production (PVGIS-SARAH3, Cuenca, 2–3 July 2023, hourly values scaled by 1.027) at 105.6 V. From top: PV power with supervisory state and thresholds; stack current and its target; cell temperature of the central and hottest segment and stack inlet temperatures; plant electricity demand and its coverage by the PV and by the grid.

The central segment of the cell, used by the control, stayed between 714 and 774 °C. The fourth segment along the flow was the hottest at full load and reached 781.2 °C, exceeding the 780 °C upper limit of the nominal range by at most 1.2 K in two excursions, 3.1 h in total; the same segment reaches 783.2 °C in four excursions, 10.9 h in total, in the reference scenario, where the plateaus at 256 A are longer. The air-side reference was at

its 780 °C bound for less than 2 min; the air heater never saturated and the sweep air stayed at the blower minimum throughout. The PV covered 233 of the 452 kWh demanded by the plant, a self-sufficiency of 52%, with 219 kWh imported from the grid and 14 kWh of PV unused, 12 kWh of which was in hot standby. The self-sufficiency was lower than in the reference scenario, 65%, because the July peaks of 20–21 kW were well below the 30.6 kW demanded at full load, and the specific demand rose to 46.0 kWh/kg, as the standby and night loads were spread over a smaller production. The supervisory logic and the cascades thus handled the satellite-derived profile without loss of thermal control, and the share of grid import is set by the ratio between PV and stack size more than by the control.

With the PV power scaled by 2 and 3, for peaks of 41.7 and 62.7 kW, production extends into the shoulders of the day, from 14.9 h to 17.7 and 20.9 h, and the stack is at 256 A for 11.3 and 14.0 h against 2.6 h with the reference field (Table 5). With the doubled field the afternoon drop still causes an excursion to hot standby, shortened to 24 min; with the tripled field it remains inside the band, and the number of transitions falls from eight to six. Hydrogen production rises to 13.23 and 15.46 kg and the specific electricity demand falls to 43.5 and 42.4 kWh/kg, as the standby and night loads are spread over a larger production. The self-sufficiency rises from 52% to 77% and 81%, while the grid import falls from 219 kWh to 131 and 126 kWh. Beyond a doubled field the additional PV thus feeds the longer full-load periods and is otherwise unused, at 49 and 211 kWh, as it exceeds the 30.6 kW demanded at full load. About a quarter of the residual import is due to the night and standby loads and the remainder to production at the shoulders of the day, mainly at partial load, when the PV is below the plant demand; it can be reduced further only by storage or by a dispatch rule tied to the PV surplus. The thermal behaviour does not depend on the field size: the central segment stays between 712 and 774 °C, the hottest segment exceeds 780 °C by at most 1.1 K, in four and three excursions whose total duration grows with the full-load hours, and the sweep air leaves the blower minimum for 26 min after the start-up, when the target rises at once, and for a few minutes in the afternoon.

3.7. Sensitivity to the Area-Specific Resistance

The uncertainties of the scale-up discussed in Section 2.4 would all appear as a change in the effective ASR. Their effect was bounded by repeating the reference scenario at 105.6 V with ASR_0 decreased and increased by 20%, to 0.264 and 0.396 Ω cm^2 at 800 °C, with E_a, the initial state and all control settings unchanged (Figure 16 and Table 6). The supervisory sequence is unaffected: the eight transitions occur at the same instants in the three runs, being driven by the PV signal alone, and the current target is met on every plateau. Hydrogen production changes by −0.8% and +2.7% with respect to the 14.07 kg of the reference, and the specific electricity demand by +0.3 and −0.4 kWh/kg. Most of the increase with the lower ASR arises in the first two hours, when the stack starts from the common initial state at 760 °C and the current overshoots to 304 A; from 09:00 of the first day the two runs differ from the reference by −0.3% and +1.2%.

Table 6. Sensitivity to the area-specific resistance at 105.6 V over the two days of the reference scenario (E_a = 80.7 kJ/mol in all runs).

Indicator	ASR_0 = 0.264 Ω cm^2 (−20%)	ASR_0 = 0.330 Ω cm^2 (Reference)	ASR_0 = 0.396 Ω cm^2 (+20%)
State transitions (production → HSB/HSB →	8 (3/2)	8 (3/2)	8 (3/2)

Indicator	ASR_0 = 0.264 Ω cm² (−20%)	ASR_0 = 0.330 Ω cm² (Reference)	ASR_0 = 0.396 Ω cm² (+20%)
production)			
Time in production/HSB/NM (h)	19.5/4.1/16.4	19.5/4.1/16.4	19.5/4.1/16.4
Hydrogen, first/second day (kg)	8.13/6.32	7.85/6.22	7.77/6.19
Hydrogen, total/from current target (kg)	14.45/13.90 (+3.9%)	14.07/13.90 (+1.2%)	13.96/13.90 (+0.4%)
Hydrogen from 09:00 of the first day (kg)	12.86	12.71	12.67
Mean |I − I_target| in production (A)	11.5	7.6	6.4
Central cell segment, min/max (°C)	700/768	713/776	727/797
Central segment, time above 780 °C (h)	0	0	14.2
Hottest segment, max (°C)/time above 780 °C (h)	777.9/0	783.2/10.9	804.6/16.1
Air reference at the 780 °C bound (h)	0.03	0.03	9.2
Fuel inlet temperature, max (°C)	771.4	776.7	796.1
References at the 700 °C floor in production (h)	4.4	2.0	0.5
Electricity demand (kWh)/PV self-sufficiency (%)	627/64.2	616/65.3	615/65.5
Specific electricity demand (kWh/kg)	43.4	43.8	44.1
Stack heater energy (kWh)/peak (kW)	17.2/2.31	17.9/2.33	19.0/2.38

The ASR sets the temperature at which the cascades find the target current. On the clear-sky plateau, 256 A is reached with the central segment at 752 °C with the lower ASR, 774 °C in the reference and 793 °C with the higher ASR. The shifts of −22 and +19 K are slightly smaller than the 25 and 21 K given at constant current density by the Arrhenius law of Equation (6), $\Delta T \approx R\,T^2\,\ln(ASR/ASR_ref)/E_a$, since the Nernst voltage decreases as the temperature rises. With the higher ASR the air-side reference reaches its 780 °C bound and the fuel-side reference settles at 793 °C, below its 800 °C bound, so that the target is held at the expense of the temperature: the central segment exceeds 780 °C for 14.2 h and the hottest segment reaches 804.6 °C. With the lower ASR the cell stays between 700 and 768 °C; the references reach the 700 °C floor during the evening ramp-down and after the cloud passages, where the current cannot be lowered further and exceeds its target, and the mean deviation in production rises to 11.5 A.

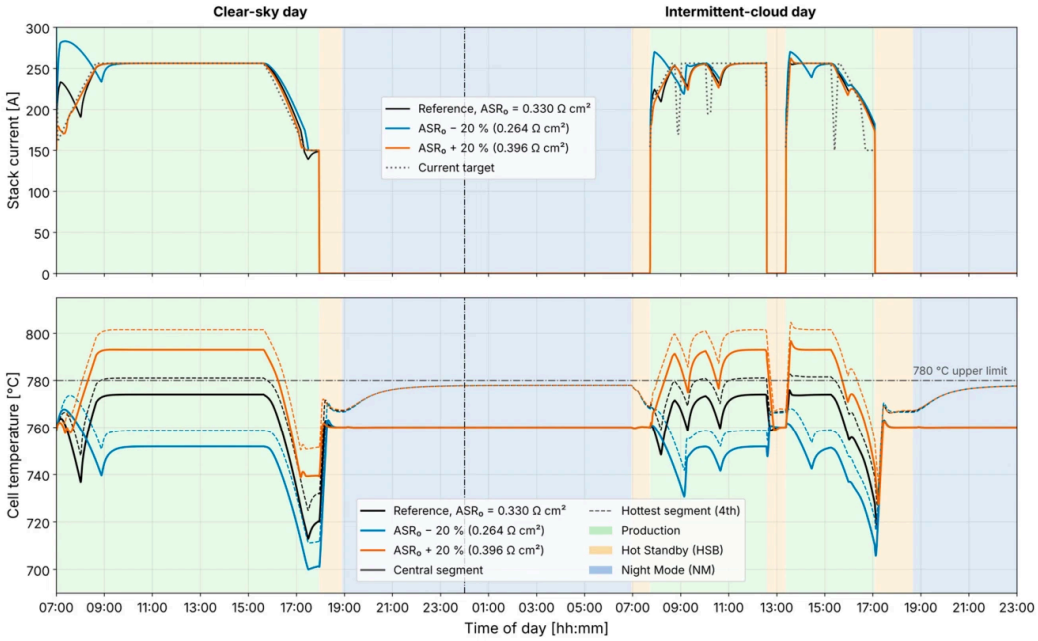


Figure 16. Sensitivity to the area-specific resistance (ASR_0 = 0.264, 0.330 and 0.396 Ω cm^2 at 800 °C) at 105.6 V over the two days. **Top**: stack current and its target. **Bottom**: cell temperature of the central segment (solid) and of the hottest segment (dashed).

The strategy is therefore robust to the uncertainty of the ASR in its supervisory and production performance, whereas the temperature margin depends on it directly: an effective ASR 20% above the calibrated value moves the full-load operating point at 1.32 V/cell beyond the nominal range. The stack voltage, or the full-load current target, has thus to be matched to the effective ASR identified at commissioning, the same adaptation that stack degradation requires over the operating life. A lower ASR only reduces the turndown available at 1.32 V/cell, which the floor of the references converts into a small excess of production.

3.8. Positioning with Respect to Other Flexible Operation Strategies

Table 7 positions the constant-voltage, temperature-tracking strategy against the other schemes proposed for flexible SOEC and rSOC operation, on the dimensions that matter for a PV-dispatched plant: the variable through which the load is modulated, the response time, the steam utilisation, the temperature margin, the auxiliary consumption and the way state transitions are handled. The current-controlled schemes of the stack-level literature [17,19,20,36] act on the load in seconds and leave the thermal management to the sweep air or to a model-based controller; they offer the fastest tracking, at the price of air flows and blower powers that grow with the current and of a temperature margin that depends on the controller. The first option of the test campaign [22] keeps the stack at constant voltage and temperature and modulates the load through the steam flow, so that the utilisation follows the load and the response is bounded by the steam generator and the lamination valve, with a risk of starvation at low flow. The second option, implemented here, fixes the steam per state and tracks the current through the inlet temperatures: the response is of the order of minutes, bounded by the 0.05 K/s ramps and the stack inertia; the utilisation is set by the two steam levels; the temperature margin is explicit through the 700–780/800 °C references and the floor; and the auxiliary consumption is the lowest of the three, since at the heat-balance point the heaters are nearly idle and the sweep air is at its minimum. Its limitation, exposed in Section 3.2, is the absence of an intrinsic current limit, which the current-controlled schemes have by

construction.

Table 7. Positioning of the constant-voltage, temperature-tracking strategy against the other flexible operation schemes of the literature.

Scheme	Load Manipulated Through	Response	Steam Utilisation	Temperature Margin	Auxiliary Consumption	State Transitions	Refs.
Constant voltage, temperature tracking (this work)	Stack inlet temperatures via fuel and air heaters (cascades CL7, CL8)	Minutes: 0.2 A/s target ramp, 0.05 K/s references, stack inertia	Fixed per state by two steam levels (54–92%)	Explicit: references bounded at 700–780/800 °C and floored at the cell temperature	Lowest: heaters nearly idle at the heat-balance point, sweep air at minimum	Production, HSB and NM with hysteresis; sweep-air loop disabled outside production	This work, [22]
Constant voltage, steam tracking	Steam flow to the stack at fixed stack temperature	Tens of minutes: steam generator and lamination valve dynamics	Varies with load; starvation risk at low flow	Implicit: stack temperature held constant	Steam generation and fuel heater duty follow the load	Same supervisory states	[22]
Current control with thermal management by sweep air	Stack current setpoint; temperature regulated by air flow	Seconds on the current; thermal response set by the air loop	Set by the steam-to-current ratio	Depends on the air-loop tuning; thermal gradients at high current	Blower power grows with the current	Stack-level studies; transitions not resolved at plant level	[19,36]
Model-based current and temperature control	Current and temperatures through a control-oriented model	Fastest; limited by the model fidelity	Controlled explicitly	Constraint-handled by the controller	Depends on the formulation	Stack or module level	[17,20]
Reversible (rSOC) mode switching	SOEC–SOFC reversal through hot standby	Paced by the thermal inertia at reversal	Mode-dependent	Thermal cycling at each reversal	Fuel-cell heat available in SOFC mode	Hot standby mediates the change of mode	[19,36]

The reversible schemes [19,36] add the SOEC–SOFC reversal, which the present plant does not contemplate, but the mechanism they rely on is the same hot standby that bridges production and night here: the stack is kept at temperature with the current removed, and the transition is paced by the thermal inertia. The supervisory logic of Section 2.6, with its hysteresis bands and the state-dependent handling of the sweep-air loop, is therefore transferable to rSOC plants, where the HSB would also mediate the change of mode; the requirement to disable the sweep-air loop outside production applies there with the same force, since the fuel-cell mode releases heat that the SOEC mode does not.

4. Conclusions

An equation-based dynamic model of the complete BoP of the 25 kW PROMETEO solid oxide electrolyser has been developed in Modelica, with a stack model validated on 5 kW experimental data from the FBK laboratories and scaled up to 25 kW as a preliminary estimate. The ten-loop constant-voltage, temperature-tracking strategy and a PV-dispatched supervisory state machine with hysteresis were verified over a clear-sky and an intermittent-cloud day. With the stack thermal capacity of 25 kJ/K and the direct stack heater of the pilot, 1.32 V/cell is the heat-balance point of the stack: the sweep-air loop rests at the blower minimum, the current is tracked through the inlet temperatures alone, and the plant electricity demand is 39.8 kWh/kg at full load and 44 kWh/kg on a daily basis, 65% of which is covered by the PV and the remainder imported from the grid under the dispatch rule adopted. The feasible voltage window, about 1.30–1.33 V/cell at the present steam levels, insulation and thermal capacity of 25 kJ/K, is narrow: at 1.28 V/cell the stack must be held above its 780 °C limit; at 1.35 V/cell and above the current becomes steam-limited and the stack overheats, so that constant-voltage operation requires a current or steam protection that the strategy does not contain; the same protection is needed at the evening ramp-down for a stack heavier than 25 kJ/K, whereas hydrogen output and consumption are otherwise insensitive to the capacity over a factor of eight. The principal design outcome concerns the sweep-air loop: kept active in hot standby and night mode, or in production with references below the stack temperature, it drives blower and heaters into saturation and cools the stack; holding the air flow at its minimum outside production, flooring the references at the stack temperature and freezing the loop while the air heater is saturated keep the stack at temperature with 2.4 kW at night. The supervisory logic handled the cloud-induced transitions, including a 48 min excursion to hot standby, without loss of thermal control, and on the satellite-derived PV production of two July days at the site it completed eight state transitions with a mean current deviation of 9 A in production and a PV self-sufficiency of 52%, which rose to 77% and 81% with the field doubled and tripled, the residual grid import being due to the night, standby and shoulder hours. A change of ±20% in ASR_0, which bounds the uncertainty of the scale-up, left the state sequence unchanged and the hydrogen production within 3% of the reference, and shifted the stack temperature at full load by about 20 K, so that the voltage setpoint had to be matched to the effective ASR identified at commissioning.

Three developments follow: a current limiter or a steam feedforward on the measured current, so that the strategy remains safe outside the window identified here, with a single outer loop feeding both temperature references; measured PV and solar-thermal time series with an explicit model of the molten-salt storage and the closure of the electrical balance; and the cross-validation of the framework against the 25 kW pilot, with degradation models added as operating hours accumulate.

Author Contributions: Conceptualisation, M.B. and M.T.; methodology, M.B.; software, M.B. and N.N.; validation, M.B.; formal analysis, M.B.; investigation, M.B.; resources, M.T. and N.N.; writing—original draft, M.B.; writing—review and editing, L.P., M.T., E.M., L.C. and N.N.; supervision, L.C.; project administration, M.T.; funding acquisition, L.C. All authors have read and agreed to the published version of the manuscript.

Funding: This research received no external funding

Data Availability Statement: The original contributions presented in this study are included in the article/. Further inquiries can be directed to the corresponding author(s).

Acknowledgments: This project has received funding from the Fuel Cells and Hydrogen 2 Joint Undertaking (now Clean Hydrogen Partnership) under Grant Agreement No 101007194. This Joint Undertaking receives support from the European Union's Horizon 2020 Research and Innovation program, Hydrogen Europe and Hydrogen Europe Research. During the preparation of this manuscript, the authors used Claude (Anthropic; Claude Sonnet 5) for the purposes of editing the text, generating the plotting scripts of the result figures from the simulation outputs and drafting the explanatory diagram of Figure 6b, as described in Section 2.8. The authors have reviewed and edited the output and take full responsibility for the content of this publication.

Conflicts of Interest: Author Nirmala was employed by the company Modelon AB. The remaining authors declare that the research was conducted in the absence of any commercial or financial relationships that could be construed as a potential conflict of interest.

Abbreviations

Symbol	Meaning
ASR	Area-specific resistance
BoP	Balance of plant
CF, CF_f	Capacity factor of the PV plant, raw and filtered
CL	Control loop
CS	Specific electricity consumption
HSB	Hot standby
HTF	Heat transfer fluid
NM	Night mode
PV	Photovoltaic
RES	Renewable energy sources
SH	Stack heater control loop
HEX	Heat exchanger
SOEC	Solid oxide electrolysis cell
TES	Thermal energy storage
WKO	Water knock-out

Appendix A. BoP Model Components

Table A1. BoP model components and modelling approach (numbering as in Figure 2 of the main text).

No.	Component	Modelling Approach
1	PK104: SOEC stack module	1D, N = 5 volumes; electrochemical cell model, anode/cathode channels, insulation heat losses
2	E102: steam generator	Shell-and-tube gas/two-phase exchanger, lumped-pressure pipes, dynamic wall
3	E104: air pre-heater	Distributed counter-flow gas/gas exchanger, N = 3, dynamic wall
4	E103: feed/effluent HEX	Distributed counter-flow

No.	Component	Modelling Approach
		gas/gas exchanger, N = 3, dynamic wall
5	EK101: feed electric heater	Prescribed heat flow, PI-controlled (CL7)
6	EK102: electric air heater	Prescribed heat flow, PI-controlled (CL8)
7	Chiller	Pipe with constant heat-transfer coefficient and prescribed cooling duty (P control)
8	WKO: water knock-out	Lumped condensing separator (0D)
9	Back-pressure valve	Algebraic valve, opening from CL9
10	Recirculation blower	Prescribed pressure ratio and isentropic efficiency, no characteristic map (CL10; Appendix G)
11	Steam lamination valve	Algebraic valve, opening from CL2
12	E101: demi-water pre-heater	Lumped economiser
13	Three-way valve	Algebraic split valve, opening from CL5
14	MX101: mixer	Lumped adiabatic mixing volume
–	Steam drum	Two-phase drum with metal thermal mass (0D)
–	Air blower (sweep air)	Ideal mass-flow source bounded at 0.002–0.040 kg/s; electrical power estimated from the network pressure drop, Equation (15)

Appendix B. Transition Logic of the Supervisory State Machine

Table A2. Transition logic of the supervisory state machine (CF_f: filtered capacity factor; nominal thresholds CF = 0.10 between NM and HSB and CF = 0.30 between HSB and production).

Transition	From → To	Condition	Hysteresis	Setpoints Issued to the Control Loops
tr_endNightMode	NM → HSB	CF_f > 0.25	Nominal + 0.15	Steam flow to the HSB level (CL2, 1.50 g/s); forming-gas purge stopped and H_2 make-up resumed; recirculation to

Transition	From → To	Condition	Hysteresis	Setpoints Issued to the Control Loops
				the HSB level (CL5); heater and stack-heater references held at 760 °C; stack disconnected; air flow at the blower minimum.
tr_toProduction	HSB → Production	CF_f > 0.50	Nominal + 0.20	Stack connected at 105.6 V (CL1); current target from Equation (12), ramped at 0.2 A/s from 150 A; heater references taken over by the cascades CL7 and CL8 and stack-heater setpoint by the fuel-side reference; CL6 enabled with ΔT = 15 K; steam flow to the level of the current target (CL2).
tr_endProduction	Production → HSB	CF_f < 0.15	Nominal − 0.15	Current target ramped down to 150 A, then stack disconnected (CL1); heater and stack-heater references ramped to 760 °C; CL6 frozen and air flow ramped to the blower minimum; steam flow to the HSB level; H_2 make-up from bottles (CL5).
tr_toNightMode	HSB → NM	CF_f < 0.02	Nominal − 0.08	Steam flow

Transition	From → To	Condition	Hysteresis	Setpoints Issued to the Control Loops
				ramped to zero and lamination valve closed (CL2); forming-gas purge 20/80 H_2/N_2 and recirculation to the NM level (CL5); heater and stack-heater references held at 760 °C; stack disconnected; air flow at the blower minimum.

Appendix C. Calibration of the Air Pre-Heater E104

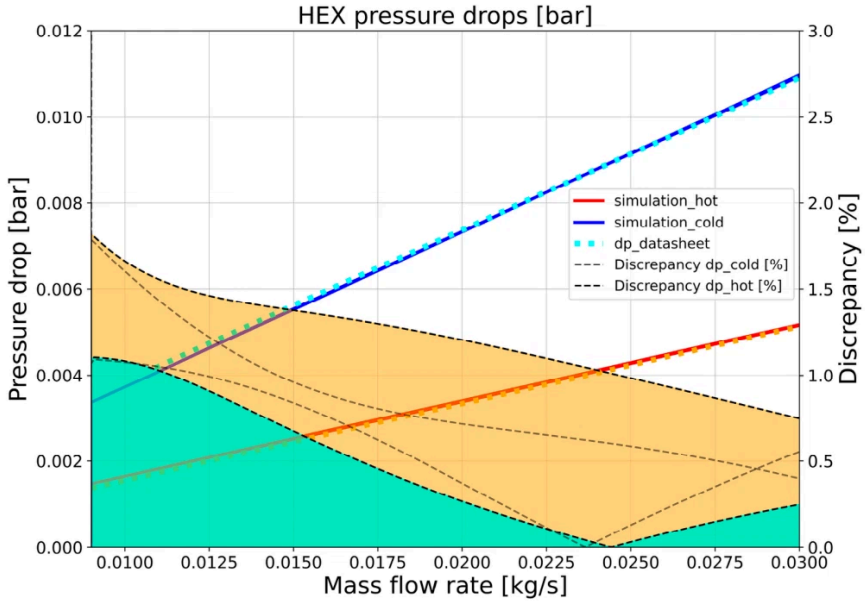
For the first calibration of the air pre-heater E104 the datasheet of the plate heat exchanger supplied for the pilot was considered, although it refers to an air-flow range from 32.4 to 108 kg/h (0.009 to 0.030 kg/s), narrower than the range spanned by the simulations. The datasheet conditions are reported in Table A3.

Table A3. Plate heat exchanger E104: datasheet conditions at minimum and maximum air flow.

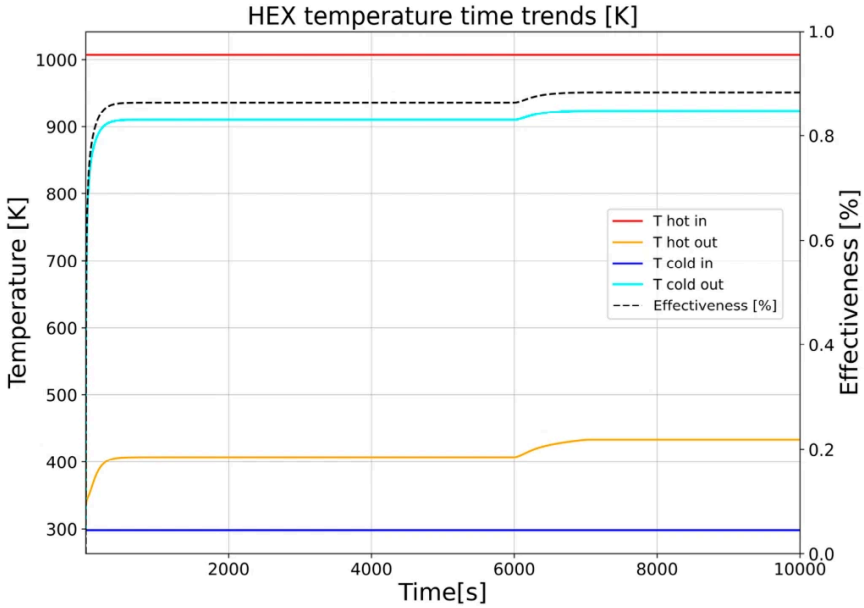
Quantity	Unit	Minimum Flow	Maximum Flow
Cold-side pressure	bar (a)	1.30	1.30
Hot-side pressure	bar (a)	1.04	1.04
Cold-side mass flow	kg/s	0.009	0.030
Hot-side mass flow	kg/s	0.009	0.032
Cold-side inlet temperature	°C	25	25
Cold-side outlet temperature	°C	629	667
Hot-side inlet temperature	°C	734	734
Hot-side outlet temperature	°C	146	142
Exchanged heat	kW	5.75	20.47
Cold-side pressure drop	mbar	3.4–3.5	11.6–12.7
Hot-side pressure drop	mbar	0.9–1.0	5.2–5.8
Core volume	l	9.1	9.1

The heat-transfer and friction sub-models of the primary and secondary channels were calibrated against these conditions by adjusting the exchange area and the length

of the discretised channels and the correction factors of the heat-transfer and pressure-loss correlations, so that the outlet temperatures and the pressure drops at the two datasheet points were reproduced. Figure A1a shows the resulting pressure drops on the two sides as a function of the air mass flow, compared with the datasheet values; the discrepancy stays within 2% over the datasheet range. Figure A1b illustrates the thermal response to a ramped increase in the air mass flow from 0.008 to 0.030 kg/s applied between 6000 and 7000 s: following the transient, the cold-side outlet temperature rises by about 15 K and the hot-side outlet by about 25 K, while the effectiveness increases from 86 to 88%, reflecting the improved thermal performance at higher flow rate.



(**a**)



(**b**)

Figure A1. (**a**) Pressure drops of E104 on the two sides as a function of the air mass flow, simulation against datasheet values, with the discrepancy on the right axis; (**b**) inlet and outlet temperatures and effectiveness during the calibration transient.

Appendix D. Stack Specifications

Table A4 lists the specifications of the 25 kW stack module provided by SolydEra and used in the model.

Table A4. Specifications and design parameters of the SOEC stack module.

Specification	Unit	Value
Full power	kW	25
Thermoneutral cell voltage at full power (manufacturer data)	V/cell	1.28
Operating voltage in the model (CL1)	V/cell	1.32
Number of cells	–	80
Active cell area	cm^2	320
Insulation thickness (Microtherm)	cm	13
Insulation density	kg/m^3	240
Insulation thermal conductivity	W/(m K)	0.04
Stack thermal capacity used in Equation (A2), 50 kg at 500 J/(kg K)	kJ/K	25

Appendix E. Cell Energy Balance

The partial pressures of reactants and products are evaluated with Equation (A1) in each segment of the one-dimensional discretisation, with a penalty function preventing negative values:

$$p_{H_2O} = p_{cath} y_{H_2O}; \quad p_{H_2} = p_{cath} y_{H_2}; \quad p_{O_2} = p_{an} y_{O_2} \tag{A1}$$

T_cell is the cell temperature, connected to the thermal port of the wall (wall.T = T_cell) so that temperature and heat-flow continuity are ensured. Equation (A2) gives the energy balance of each discretisation element:

$$\frac{M_{cp}}{N} \frac{dT_{cell}}{dt} = Q_{an} + Q_{cath} + Q_{wall} + Q_{cell} \tag{A2}$$

where M_cp is the thermal capacity of the lumped stack, 25 kJ/K for 80 cells (50 kg of cell and interconnect material at 500 J/(kg K), consistent with the 0.3–0.5 kJ/K per cell of planar SOC stacks reported in the literature [29,37]), distributed over the N segments; Q_an and Q_cath are the heat flows between the cell and the anode and cathode channels; Q_cell is the heat generated in the i-th element; and Q_wall is the heat exchanged with the external environment through the insulation model. The channel heat flows are defined with Equation (A3), where k_c = 250 $W/(m^2 K)$ is the heat-transfer coefficient between fluid and substrate:

$$Q_{an} = k_c \frac{n_{cell} A_{cell}}{N} \left(T_{wall,an} - T_{cell} \right), \qquad Q_{cath} = k_c \frac{n_{cell} A_{cell}}{N} \left(T_{wall,cath} - T_{cell} \right) \tag{A3}$$

The species mass flows through the mass ports are positive for substances entering the element (H_2O) and negative for those leaving it (H_2, O_2). The bulk enthalpy flows of the cathode and anode mixtures follow from the specific enthalpies of the species (Equation (A4)), and Q_cell is obtained from the energy balance of Equation (A5), where P_cell = V_cell I is the electrical power of the element and V_cell the potential difference between the two electric ports of the elementary cell:

$$\dot{H}_{cath} = \sum_i \dot{m}_i h_i \quad (i = H_2, H_2O), \qquad \dot{H}_{an} = \dot{m}_{O_2} h_{O_2} \tag{A4}$$

$$Q_{cell} = \dot{H}_{cath} + \dot{H}_{an} + P_{cell}, \qquad P_{cell} = V_{cell} I \tag{A5}$$

Appendix F. Model Parametrisation

Table A5 compiles the discretisation, geometry, gas volumes and thermal parameters of the BoP components, as set in the model. Values marked with an asterisk are calibration or preliminary values to be confirmed against the as-built pilot.

Table A5. Discretisation and parametrisation of the BoP model components.

Component	Discretisation	Geometry and Volumes	Thermal Parameters
SOEC stack (PK104)	1D, N = 5 elements per channel	80 cells × 320 cm^2; anode and cathode channels L = 0.11 m, D_h = 1.55 mm, gas volume 16.6 cm^3 per channel	Stack thermal capacity 25 kJ/K (50 kg × 500 J/(kg K)) over the five segments; k_c = 250 W/(m^2 K); insulation 0.13 m Microtherm on top, bottom and sides (A = 1, 1 and 2 m^2), k = 0.04 W/(m K), external convection 12 (top) and 5 (side) W/(m^2 K), emissivity 0.04; ASR_0 = 0.330 Ω cm^2 at 800 °C, E_a = 80.7 kJ/mol [21]
E104 air pre-heater	1D counter-flow, N = 3	Exchange area 10 m^2 (secondary) and 1 m^{2*} (primary), L = 0.5 m, D_h = 10 mm	Wall mass 0.3 kg*, steady-state wall initialisation; pressure-loss operating point 100 Pa at 0.003 kg/s
E103 feed/effluent HEX	1D counter-flow, N = 3	Channel L = 1 m, D_h = 20 mm, exchange area 0.1 m^2 per side*	Constant heat-transfer coefficient 100 W/(m^2 K)*; stainless steel 316L wall
E102 steam generator	Shell-and-tube, lumped-pressure	Primary (HTF) L = 0.8 m, D = 20 mm;	Two-phase heat-transfer coefficients

Component	Discretisation	Geometry and Volumes	Thermal Parameters
	pipes	secondary (water/steam) L = 0.8 m, D = 2 mm	3000 W/(m^2 K); primary 1500 W/(m^2 K); standard steel wall
Steam drum	0D two-phase volume	L = 1 m, r_int = 0.50 m, r_ext = 0.51 m	Metal thermal mass from steel density 8000 kg/m^3 and c_p 500 J/(kg K); setpoint 3 bar, level 0.18 m
E101 economiser	0D	Lumped water pre-heater at 3 bar	–
Chiller	Pipe, lumped	L = 1 m, D = 16 mm, V = 0.20 L	Constant coefficient 800 W/(m^2 K); duty set by P control to the WKO inlet temperature; COP 3 for the electrical equivalent
WKO/condensing separator	0D	V = 0.1 m^3	Condensation time constant 2 s
Cold-side gas volumes	0D, N = 2–4 ports	0.1 m^3 (separator outlet), 0.15 m^3 (recirculation), 2 L (blower outlet)	Isothermal at 5 °C (cold zone)
Pipes to stack (fuel, air)	Pipe, lumped	L = 1 m, D = 20 mm, V = 0.31 L each	Adiabatic
Sweep-air blower	Ideal mass-flow source	Range 0.002–0.040 kg/s	Power estimated with η_blower = 0.55, η_motor = 0.90, Equation (14)
Recirculation blower	Prescribed pressure ratio (Appendix G)	–	Isentropic efficiency 0.75; motor and transmission efficiency 0.30
Electric heaters	Prescribed heat flow	–	Limits 8 kW (electrical heater) reference ramp 0.05 K/s

Appendix G. Recirculation Blower Model

The anode recirculation blower (item 10 of Table A1) is represented by a prescribed-pressure-ratio, prescribed-efficiency model without a characteristic map, since the machine of the pilot has not been characterised yet. The mass flow through the blower is determined by the circuit, namely by the recirculation valve of CL5, and the pressure ratio PR = p_out/p_in is set by CL10 as a feedforward: the delivery pressure is kept above the measured mixer pressure by a margin proportional to the opening command of the recirculation valve (CL5), up to 150 mbar, the ratio being bounded between 1 and 1.35

and filtered with a time constant of 2 s to represent the machine response. The inlet state is evaluated from the enthalpy and composition of the incoming reformate mixture, treated as an ideal gas, and the isentropic exponent γ = c_p/c_v is evaluated at the inlet. The isentropic outlet temperature is obtained explicitly, without an inner iteration,

$$T_{is} = T_{in}\ PR^{\frac{\gamma-1}{\gamma}} \tag{A6}$$

the isentropic outlet enthalpy h_is is evaluated at the outlet pressure and T_is, and the actual outlet enthalpy follows from the isentropic efficiency η_is = 0.75, all losses being transferred to the gas:

$$h_{out} = h_{in} + \frac{h_{is} - h_{in}}{\eta_{is}}, \qquad h_{is} = h\left(p_{out}, T_{is}\right) \tag{A7}$$

The compression work is obtained from a static energy balance and converted to electrical power with a motor and transmission efficiency η_m = 0.30, a conservative value for the small machine of the pilot to be confirmed against the as-built hardware; this is the term P_c,rec/η_m of Equation (12):

$$P_{c,rec} = \dot{m}_{rec}\ \left(h_{out} - h_{in}\right), \qquad P_{el,rec} = \frac{P_{c,rec}}{\eta_m} \tag{A8}$$

Flow reversal through the blower is not supported and is asserted; the pressure ratio is bounded below at 1. The outlet composition equals the inlet composition and the blower has no thermal capacity of its own, the downstream volume (Table A5) providing the dynamics of the recirculation line.

References

1. Fang, R.; Liang, Y. Control strategy of electrolyzer in a wind-hydrogen system considering the constraints of switching times. *Int. J. Hydrogen Energy* **2019**, *44*, 25104–25111. [Google Scholar] [CrossRef]
2. Ibrahim, M.H.; Ang, S.P.; Dani, M.N.; Petra, R.; Salam, M.A. Voltage stability assessment for solar photovoltaic penetration using Reactive Power–Voltage and Active Power–Voltage modal analysis. *Energy Rep.* **2023**, *9*, 486–493. [Google Scholar] [CrossRef]
3. Schaab, K.; Hahn, J.; Wolkov, M.; Stursberg, O. Robust control for voltage and transient stability of power grids relying on wind power. *Control Eng. Pract.* **2017**, *60*, 7–17. [Google Scholar] [CrossRef]
4. Panwar, N.L.; Kaushik, S.C.; Kothari, S. Role of renewable energy sources in environmental protection: A review. *Renew. Sustain. Energy Rev.* **2011**, *15*, 1513–1524. [Google Scholar] [CrossRef]
5. Kabir, M.M.; Akter, M.M.; Huang, Z.; Tijing, L.; Shon, H.K. Hydrogen production from water industries for a circular economy. *Desalination* **2023**, *554*, 116448. [Google Scholar] [CrossRef]
6. Chi, J.; Yu, H. Water electrolysis based on renewable energy for hydrogen production. *Chin. J. Catal.* **2018**, *39*, 390–394. [Google Scholar] [CrossRef]
7. Zhou, Y.; Li, R.; Lv, Z.; Liu, J.; Zhou, H.; Xu, C. Green hydrogen: A promising way to the carbon-free society. *Chin. J. Chem. Eng.* **2022**, *43*, 2–13. [Google Scholar] [CrossRef]
8. Nemmour, A.; Inayat, A.; Janajreh, I.; Ghenai, C. Green hydrogen-based E-fuels (E-methane, E-methanol, E-ammonia) to support clean energy transition: A literature review. *Int. J. Hydrogen Energy* **2023**, *48*, 29011–29033. [Google Scholar] [CrossRef]
9. Li, X.; Raorane, C.J.; Xia, C.; Wu, Y.; Tran, T.K.N.; Khademi, T. Latest approaches on green hydrogen as a potential source of renewable energy towards sustainable energy: Spotlighting of recent innovations, challenges, and future insights. *Fuel* **2023**, *334*, 126684. [Google Scholar] [CrossRef]
10. Agaton, C.B.; Batac, K.I.T.; Reyes, E.M., Jr. Prospects and challenges for green hydrogen production and utilization in the Philippines. *Int. J. Hydrogen Energy* **2022**, *47*, 17859–17870. [Google Scholar] [CrossRef]

11. Wang, C.; Walsh, S.D.C.; Weng, Z.; Haynes, M.W.; Summerfield, D.; Feitz, A. Green steel: Synergies between the Australian iron ore industry and the production of green hydrogen. *Int. J. Hydrogen Energy* **2023**, *48*, 32277–32293. [Google Scholar] [CrossRef]
12. Zaiter, I.; Ramadan, M.; Bouabid, A.; El-Fadel, M.; Mezher, T. Potential utilization of hydrogen in the UAE's industrial sector. *Energy* **2023**, *280*, 128108. [Google Scholar] [CrossRef]
13. Zhang, F.; Zhao, P.; Niu, M.; Maddy, J. The survey of key technologies in hydrogen energy storage. *Int. J. Hydrogen Energy* **2016**, *41*, 14535–14552. [Google Scholar] [CrossRef]
14. Nnabuife, S.G.; Oko, E.; Kuang, B.; Bello, A.; Onwualu, A.P.; Oyagha, S.; Whidborne, J. The prospects of hydrogen in achieving net zero emissions by 2050: A critical review. *Sustain. Chem. Clim. Action* **2023**, *2*, 100024. [Google Scholar] [CrossRef]
15. Chen, W.; Sun, C. Recent advances in high temperature solid oxide electrolytic cells. *Energy Mater.* **2025**, *5*, 500045. [Google Scholar] [CrossRef]
16. Barelli, L.; Bidini, G.; Cinti, G. Air variation in SOE: Stack experimental study. *Int. J. Hydrogen Energy* **2018**, *43*, 11655–11662. [Google Scholar] [CrossRef]
17. Yin, R.; Sun, L.; Khosravi, A.; Malekan, M.; Shi, Y. Control-oriented dynamic modeling and thermodynamic analysis of solid oxide electrolysis system. *Energy Convers. Manag.* **2022**, *271*, 116331. [Google Scholar] [CrossRef]
18. Saeedmanesh, A.; Colombo, P.; McLarty, D.; Brouwer, J. Dynamic behavior of a solid oxide steam electrolyzer system using transient photovoltaic generated power for renewable hydrogen production. *J. Electrochem. Energy Convers. Storage* **2019**, *16*, 041008. [Google Scholar] [CrossRef]
19. Botta, G.; Romeo, M.; Fernandes, A.; Trabucchi, S.; Aravind, P.V. Dynamic modeling of reversible solid oxide cell stack and control strategy development. *Energy Convers. Manag.* **2019**, *185*, 636–653. [Google Scholar] [CrossRef]
20. Zhang, R.; Jiang, P.; Zhu, Y. Control-oriented modeling and dynamic behavior analysis of a solid oxide electrolysis cell hydrogen production system. *Fuel* **2025**, *390*, 134648. [Google Scholar] [CrossRef]
21. Barreto, G.; Romero, M.; González-Aguilar, J.; Giaconia, A.; Testi, M. Design point, part load and annual performance analysis of a 100 kW SOEC system integrating a solar steamer under electrolyser operational constraints. *Renew. Energy* **2026**, *256*, 124340. [Google Scholar] [CrossRef]
22. Crespi, E.; Panaccione, F.; Ragaglia, D.; Testi, M. Integration of a solid oxide electrolysis system with solar thermal and electrical energy: A testing campaign for operation and control strategy definition. *IET Renew. Power Gener.* **2024**, *18*, 4399–4413. [Google Scholar] [CrossRef]
23. Fritzson, P.; Engelson, V. Modelica—A unified object-oriented language for system modeling and simulation. In *ECOOP'98—Object-Oriented Programming*; Jul, E., Ed.; Springer: Berlin/Heidelberg, Germany, 1998; pp. 67–90. [Google Scholar] [CrossRef]
24. Modelon Impact: Systems Modeling and Simulation Platform. Available online: https://www.modelon.com/modelon-impact/ (accessed on 23 June 2026).
25. McBride, B.J.; Zehe, M.J.; Gordon, S. *NASA Glenn Coefficients for Calculating Thermodynamic Properties of Individual Species*; NASA Glenn Research Center: Cleveland, OH, USA, 2002. Available online: https://ntrs.nasa.gov/api/citations/20020085330/downloads/20020085330.pdf (accessed on 23 June 2026).
26. Modelica: Media—Water—StandardWater. Available online: https://doc.modelica.org/Modelica%204.0.0/Resources/helpWSM/Modelica/Modelica.Media.Water.StandardWater.html (accessed on 23 June 2026).
27. Therminol 66 Heat Transfer Fluid. Available online: https://www.eastman.com/en/products/product-detail/71093438/therminol-66-heat-transfer-fluid (accessed on 23 June 2026).
28. Sigfridsson, S.; Li, L.; Runvik, H.; Gohl, J.; Joly, A.; Soltesz, K. Modeling of fuel cell hybrid vehicle in Modelica: Architecture and drive cycle simulation. In Proceedings of the 2nd Japanese Modelica Conference, Tokyo, Japan, 17–18 May 2018; pp. 91–98. [Google Scholar] [CrossRef]
29. Petipas, F.; Brisse, A.; Bouallou, C. Model-based behaviour of a high temperature electrolyser system operated at various loads. *J. Power Sources* **2013**, *239*, 584–595. [Google Scholar] [CrossRef]
30. Andersson, D.; Åberg, E.; Eborn, J.; Yuan, J.; Sundén, B. Dynamic modeling of a solid oxide fuel cell system in Modelica. In Proceedings of the 8th International Modelica Conference, Dresden, Germany, 20–22 March 2011; pp. 593–602. [Google Scholar] [CrossRef]
31. Provatas, V.; Dapontis, S.; Konsolakis, M.; Ipsakis, D. Modeling and control of hydrogen production systems through water electrolysis and RES power. *Proceedings* **2024**, *105*, 51. [Google Scholar] [CrossRef]

32. Mewada, Y.; Prajapati, S.; Hakani, R. System for PID control and autotuning PID using Ziegler–Nichols method. *Influ. Int. J. Sci. Rev.* **2022**, *4*, 249–253. [Google Scholar] [CrossRef]
33. Yucelen, T.; Kaymakci, O.; Kurtulan, S. Self-tuning PID controller using Ziegler–Nichols method for programmable logic controllers. *IFAC Proc. Vol. 2006*, 11–16. [CrossRef]
34. Huba, M.; Chamraz, S.; Bistak, P.; Vrancic, D. Making the PI and PID controller tuning inspired by Ziegler and Nichols precise and reliable. *Sensors* **2021**, *21*, 6157. [Google Scholar] [CrossRef]
35. European Commission; Joint Research Centre. Photovoltaic Geographical Information System (PVGIS), PVGIS-SARAH3 Hourly Radiation Database. Available online: https://re.jrc.ec.europa.eu/pvg_tools/en/ (accessed on 2 October 2026).
36. Motylinski, K.; Kupecki, J.; Numan, B.; Hajimolana, Y.S.; Venkataraman, V. Dynamic modelling of reversible solid oxide cells for grid stabilization applications. *Energy Convers. Manag.* **2021**, *228*, 113674. [Google Scholar] [CrossRef]
37. Aguiar, P.; Adjiman, C.S.; Brandon, N.P. Anode-supported intermediate temperature direct internal reforming solid oxide fuel cell. I: Model-based steady-state performance. *J. Power Sources* **2004**, *138*, 120–136. [Google Scholar] [CrossRef]

Disclaimer/Publisher's Note: The statements, opinions and data contained in all publications are solely those of the individual author(s) and contributor(s) and not of MDPI and/or the editor(s). MDPI and/or the editor(s) disclaim responsibility for any injury to people or property resulting from any ideas, methods, instructions or products referred to in the content.